Signal-Level Models of Pointwise Electromagnetic Exposure for Millimeter Wave Communication

Miguel R. Castellanos, *Student Member, IEEE*, Yanan Liu, David J. Love, *Fellow, IEEE*, Borja Peleato, *Member, IEEE*, Jian-Ming Jin, *Fellow, IEEE*, Bertrand M. Hochwald, *Fellow, IEEE*

***Abstract*—Electromagnetic exposure from wireless devices is strictly regulated around the world to ensure the safety of consumers. Recent studies have demonstrated that multi-antenna systems can leverage signal-level exposure models to jointly mitigate user radiation absorption and achieve high data rates. This is especially important for millimeter wave technologies, which are susceptible to power back-off techniques due to high propagation and blockage losses. However, prior models require significant overhead in the form of exposure measurements to compute model parameters and cannot be easily modified to predict electromagnetic absorption in different testing configurations. This paper proposes methods to approximate the characteristic matrix of a quadratic model for two exposure measures in the millimeter wave band: incident power density and surface specific absorption rate (SAR). The presented models can be calculated with a small number of parameters and can be altered to account for mutual coupling, near-field effects, and changes in the exposure scenario. Spatial sampling schemes based on these models are derived to determine how many testing points are necessary to estimate exposure in a region within a specified margin of error. Software simulation results with half-wave dipoles validate the accuracy of the proposed models in a millimeter wave scenario.**

***Index Terms*—5G communication, millimeter wave communication, electrogmagnetic absorption, specific absorption rate (SAR), power density (PD), spatial sampling.**

I. Introduction

Millimeter wave technologies will play a pivotal role in meeting the large throughput demands of fifth-generation (5G) wireless communication systems [2]–[4]. Millimeter wave frequencies are ideal candidates for wireless backhaul and access in small cell deployments due to the short-range and highly directional nature of millimeter wave propagation [5], [6]. Additionally, millimeter wave vehicular communication systems can take advantage of high data rate transmissions to exchange raw, high-resolution sensor data obtained from radars, cameras, and LIDARs (LIght Detection and RAnging) [7], [8]. One key consideration for millimeter wave communication is the design of beamforming schemes that are tailored to the sparse structure of millimeter wave channels and the hardware limitations at these carrier frequencies. In this context, a variety of studies have addressed practical and efficient precoding methods for millimeter wave systems [2], [5], [9]–[16]. An additional, less explored challenge in the implementation of millimeter wave systems is the measurement and regulation of electromagnetic exposure to users.

Electromagnetic waves emanating from wireless devices are absorbed by users. This absorption occurs at all frequencies, but the level of absorption and its effect on the body is frequency dependent. Although microwave radiation is non-ionizing, biological experts generally agree that adverse health effects can arise from high levels of radio frequency (RF) energy absorption [17]. Because of this, radiation exposure is regulated by governing bodies to prevent hazardous operating conditions for users, and all wireless devices must comply with exposure limits before becoming available to the public. For lower frequency systems, both the Federal Communications Commission (FCC) and the International Commission on Non-Ionizing Radiation Protection (ICNIRP) have adopted specific absorption rate (SAR) as the standard metric for regulatory compliance [18], [19]. SAR measures user electromagnetic exposure as absorbed power per unit mass, with units W/kg. At frequencies between 100 KHz and 6 GHz, the FCC SAR limit for RF exposure from portable devices used by the public is a 1.6 W/kg average over any one gram of tissue [20].

Millimeter wave absorption behaves differently than absorption at sub-6 GHz frequencies, and its regulation requires the use of alternative exposure metrics. The limited penetration of millimeter waves into the body leads to a large concentration of energy deposition in thin layers of exposed tissue such as the skin and the eye, but negligible absorption a few millimeters below the surface [21]. As a result, tissue heating from millimeter wave exposure is largely restricted to a thin tissue layer and is typically measured with superficial quantities such as incident power density (PD) and SAR at the tissue surface, commonly referred to as surface SAR.

Electromagnetic emission management is critical to the safety and success of millimeter wave systems. Studies have shown that incident PD levels above several hundred mW/cm^2 can cause pain in the skin and even ocular lesions [22]. Recent works related to 5G exposure have addressed the effects of exposure constraints on millimeter wave devices and the advantages of exposure-aware system design [23]–[26]. Regardless, exposure constraints are typically ignored during

This work was supported in part by the National Science Foundation under grants CCF-1403458 and CNS-1642982. Our initial results were presented in Asilomar 2016, Pacific Grove, CA, USA [1].

M. R. Castellanos, D. J. Love, and B. Peleato are with the School of Electrical and Computer Engineering, Purdue University, West Lafayette, IN 47907 USA (e-mail: castellm@purdue.edu; djlove@purdue.edu; bpeleato@purdue.edu).

Y. Liu and J.-M. Jin are with the Center for Computational Electromagnetics, Department of Electrical and Computer Engineering, University of Illinois at Urbana-Champaign, Urbana, IL 61801, USA (e-mail: yliu258@illinois.edu, j-jin1@illinois.edu).

B. M. Hochwald is with the Department of Electrical and Computer Engineering, University of Notre Dame, Notre Dame, IN 46556 USA (e-mail: bhochwal@nd.edu).

system design and later act as secondary power constraints if absorption measurements exceed existing thresholds. Such power limits on user-end devices can cause significant degradation to the system performance, especially since millimeter wave systems need high transmit gains to combat path loss. Fortunately, multiple-input multiple-output (MIMO) communication systems can benefit from large exposure variations as a function of signal design and are able to jointly maximize the achievable rate under exposure constraints.

A number of studies have addressed the development, validation, and application of signal-level exposure models. SAR measurement variations with respect to the phase difference between two transmit antennas were first addressed in [27], [28]. Work in [29]–[32] later demonstrated that SAR can be approximated as a mixed quadratic function of the transmit signal and introduced the notion of an *exposure matrix*, which is the characteristic matrix in the quadratic model. A Fourier analysis based model for fast SAR and power loss density estimation was also proposed and validated in [33]. In [34], [35], a method for determining device compliance with SAR limits in linear time was derived by exploiting the structure of the quadratic model. Not only are these models important for characterizing the exposure induced by wireless devices, but they also can be incorporated as constraints on signaling methods to achieve exposure-aware transmissions [1], [29]–[31], [36]–[39]. While the aforementioned quadratic model can predict electromagnetic exposure with high accuracy, computing the model parameters requires a significant amount of overhead in the form of exposure measurements from software simulations or phantom head setups.

Main Contributions: This work addresses the issue of constructing low-complexity models for incident PD and surface SAR in the millimeter wave band by deriving formulas to approximate the exposure matrices in the quadratic model proposed in [29]–[32]. With this goal in mind, we leverage the relative simplicity of electromagnetic absorption measures adopted for millimeter wave communication to develop parametric expressions that only require a few external measurements and that can easily adapt to the testing configuration. We note that the proposed models can be applied to other frequency bands, but the considered exposure scenario and measures are mostly relevant to millimeter wave systems at this time, meaning that the efficacy of the proposed model outside of the millimeter wave band is unclear.

We develop a method to calculate incident PD matrices by approximating the near-field gain of the transmitter in terms of basic array parameters and incorporating existing models for mutual coupling and near-field effects. We also derive an expression for SAR matrices by modeling the total electric field transmitted through the air-tissue boundary as the superposition of incident spherical waves refracted as plane waves through a planar dielectric. The proposed formulas for the characteristic exposure matrices demonstrate how the quadratic model can be represented as a rank-one model in terms of an effective steering vector, which is defined later. To validate the model, we simulate a 28 GHz millimeter wave exposure scenario with a uniform linear array (ULA) composed of half-wave dipoles and a spherical tissue model. Our results demonstrate a high degree of agreement between the quadratic model with the calculated exposure matrices and the simulation values.

The proposed models estimate pointwise exposure and are therefore not directly compatible with regulatory thresholds, which are defined as averages over predetermined areas or volumes. Therefore, a key modeling consideration is how to sample a spatial region to obtain a robust characterization of averaged exposure. We first derive upper bounds on the exposure differential between two testing points based on the proposed models. This result is used to develop uniform and non-uniform spatial sampling guidelines which describe how to separate adjacent sample points so that the difference in the exposure levels at these points does not exceed a predetermined threshold. We also discuss how to construct exposure models for average exposure from the sampled pointwise models. Finally, we present numerical examples to demonstrate the application of the developed sampling methods, and validate the average exposure model.

Organization: This paper is organized as follows. In Section II, we review prior work on signal-level exposure modeling and outline our proposed approaches for computing exposure matrices in the millimeter wave band. The proposed millimeter wave exposure models are developed in detail in Section III. Section IV presents software simulation results of a simple millimeter wave exposure scenario to validate the proposed models. Spatial sampling techniques and the characterization of spatially averaged exposure are discussed in Section V.

Notation: A bold lowercase letter $\mathbf{a}$ denotes a column vector, a bold uppercase letter $\mathbf{A}$ denotes a matrix, $\mathbf{A}^T$ denotes the transpose of $\mathbf{A}$, $\mathbf{A}^H$ denotes the conjugate transpose of $\mathbf{A}$, $\|\mathbf{a}\|$ denotes the vector 2-norm of $\mathbf{a}$, $\|\mathbf{A}\|_2$ denotes the induced vector 2-norm of $\mathbf{A}$.

II. Procedures for Computing Signal-Level Exposure Models

We briefly review the results of prior exposure modeling studies in [29]–[33] and define the notion of an exposure matrix. We then present our proposed procedures for calculating exposure matrices for pointwise incident PD and surface SAR. The measurements required to compute exposure matrices with both the prior and the proposed methods are discussed and compared.

A. Review of Prior Art

Wireless devices sold worldwide are thoroughly tested for compliance with regulatory standards for maximum user exposure. These limits are often set conservatively to ensure that electromagnetic radiation absorbed by users does not cause biologically significant thermal heating. For systems operating below 6 GHz, exposure measurements are typically expressed in terms of SAR. SAR is a measure of power absorbed in human tissue per unit mass at a point $\mathbf{p}$ and is expressed as

$$\mathrm{SAR}(\mathbf{p}) = \frac{\sigma\left|\mathcal{E}_m(\mathbf{p})\right|^2}{2\rho}, \tag{1}$$

where σ is the tissue conductivity, $\mathcal{E}_m(\mathbf{p})$ is the electric field strength, and ρ is the density of the tissue [40].

In a multi-antenna system, SAR values can vary significantly with respect to the transmit signal. Let N be the number of transmitter antennas, and let $\mathbf{x}$ be the length N transmit signal vector. Experimental results in [29]–[33] show that average SAR measurements over a volume V are well approximated as a quadratic function of the transmit signal $\mathbf{x}$ as

$$\mathrm{SAR}_V(\mathbf{x}) = \mathbf{x}^H \mathbf{R}_V \mathbf{x}, \tag{2}$$

where $\mathbf{R}_V$ is the $N \times N$ matrix that characterizes the variation of SAR with respect to $\mathbf{x}$ within the volume. Various studies have shown that incorporating SAR constraints into signal design problems by employing the quadratic model yields significantly higher rates compared to conventional power back-off schemes which lower the transmit power to satisfy exposure constraints [29]–[31], [36]–[39].

In (2), the SAR matrix $\mathbf{R}_V$ is obtained by a fitting method, such as a least-squares algorithm, on measured SAR data. Since regulatory agencies place limits on the worst-case exposure, the volume is chosen such that it corresponds to the maximum region of absorption. Changing the transmission frequency or the location of the wireless device relative to the body can change the location of the hotspot [31]. Therefore, different operating conditions must be modeled by different SAR matrices, all of which require additional exposure data.

Constructing sub-6 GHz SAR models requiring less measurements/simulations is challenging given the complex nature of electromagnetic absorption at these frequencies. Electromagnetic radiation at lower frequencies can reach past the dermal and subcutaneous skin layers, and maximum SAR measurements are typically found inside the body. For example, emissions from a portable device operating near the head often induce SAR hotspots inside of the skull. Cooling mechanisms such as blood flow can also significantly reduce intrabody tissue heating and affect the location of maximum exposure.

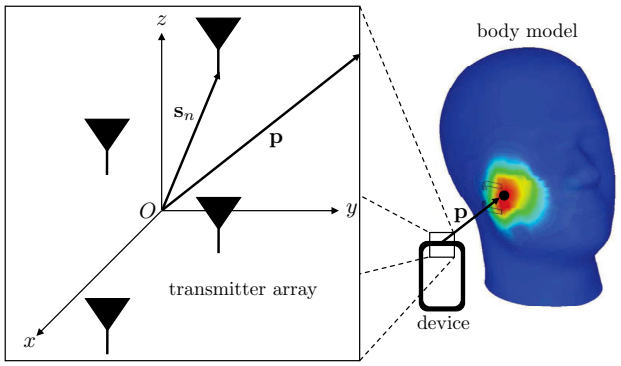

Fig. 1. A diagram of the considered exposure scenario. A body model lies close to an N element transmitter array. The position of the n-th element is $\mathbf{s}_n$, and exposure is measured at a point $\mathbf{p}$ on the body surface.

In contrast, the submillimeter penetration depths of millimeter waves lead to extremely large local SAR values at the tissue surface [21]. The superficial nature of millimeter wave absorption suggests tissue heating is heavily dependent on incident PD and surface SAR levels, which are markedly easier to understand and model than SAR readings at points deep in the body.

In the remainder of this study, we construct and analyze low-complexity signal-level models for incident PD and surface SAR by exploiting the simple nature of these exposure measures. Although these models are valid at all frequencies, the main motivation for this work is to develop signal-level models that can be easily incorporated into the design of exposure-aware transmission schemes such as those proposed in [29]–[31], [36]–[39]. As incident PD and surface SAR are not robust measures of exposure for lower frequencies, the proposed models may not be useful for this application for sub-6 GHz devices. Therefore, we mainly focus on the models in the context of millimeter wave systems.

B. Proposed Methods for Computing Exposure Matrices

Both incident PD and surface SAR are proportional to the squared electric field magnitude, therefore either dosimetric quantity can be characterized as a quadratic function of a transmit signal $\mathbf{x}$ as

$$\mathsf{EXP}(\mathbf{p}, \mathbf{x}) = \mathbf{x}^H \mathbf{R}(\mathbf{p}) \mathbf{x}, \tag{3}$$

where EXP is the exposure measure, $\mathbf{p}$ is the measurement point, and $\mathbf{R}(\mathbf{p})$ is the $N \times N$ characteristic exposure matrix for the point $\mathbf{p}$. We precede the development and justification of the proposed models by outlining how to compute the exposure matrix $\mathbf{R}(\mathbf{p})$ at a point $\mathbf{p}$. In the considered exposure scenario, an N element antenna array is in the vicinity of an arbitrary tissue model and exposure is measured at a point $\mathbf{p}$ on the body surface, as shown in Fig. 1. The position of the n-th array element and the vector from the n-th element to $\mathbf{p}$ are denoted as $\mathbf{s}_n$ and $\mathbf{p}_n = \mathbf{p} - \mathbf{s}_n$, respectively. The phase center of the array, given as $\sum_{n=0}^{N-1} \mathbf{s}_n$ [41], is assumed to lie at the origin for convenience.

Table I lists the necessary model parameters, drawing a distinction between those which are known or measured, and those which are calculated. Parameters related to the antenna gain, such as the gain patterns and the array coupling matrix, are assumed to be normalized with respect to the transmit power. Additionally, the transmit signal $\mathbf{x}$ is assumed to be unit-norm. The following procedures provide a step-by-step guides for calculating the matrix $\mathbf{R}_{\mathsf{EXP}}(\mathbf{p})$.

Procedure for Computing PD Matrices: To compute the PD matrix $\mathbf{R}_{\mathsf{PD}}(\mathbf{p})$, follow the steps below:

1) Calculate the near-field steering vector $\mathbf{a}(\mathbf{p})$, which is defined as [41]

$$\mathbf{a}(\mathbf{p}) \triangleq \left[\gamma_0 e^{-j\varphi_0} \ \gamma_1 e^{-j\varphi_1} \ \ldots \ \gamma_{N-1} e^{-j\varphi_{N-1}}\right]^{\mathsf{T}}, \tag{4}$$

where φ_n and γ_n are given by

$$\varphi_n = \frac{2\pi \left(\|\mathbf{p}_n\| - \|\mathbf{p}\|\right)}{\lambda}, \tag{5}$$

$$\gamma_n = g_n^{1/2}(\mathbf{p}_n) \frac{\|\mathbf{p}\|}{\|\mathbf{p}_n\|}. \tag{6}$$

If the gain patterns $g_n(\mathbf{p}_n)$ are near-field gain patterns, then set $\gamma_n = g_n^{1/2}(\mathbf{p}_n)$.

TABLE I
LIST OF MODEL PARAMETERS.

Measured/Known Parameters	Description
λ	Transmission wavelength (m)
$g_n(\mathbf{p})$	Gain pattern of the n-th antenna element
P	Transmit power (W)
$\alpha(\|\mathbf{p}\|)$	Near-field gain correction factor
$\mathbf{M}$	Array coupling matrix
ϵ^*	Relative complex tissue dielectric constant
ρ	Tissue density (kg/m^3)
Calculated Parameters	
$\mathbf{a}(\mathbf{p})$	Near-field steering vector
ζ_n^i	Angle of incidence from n-th source to $\mathbf{p}$
τ_n	Transmission coefficient for n-th source at $\mathbf{p}$

2) If coupling between array elements is to be modeled, determine a suitable coupling matrix $\mathbf{M}$. Otherwise set $\mathbf{M} = \mathbf{I}$.
3) If the gain patterns $g_n(\mathbf{p}_n)$ were measured in the far-field, determine an appropriate scaling coefficient $\alpha(\|\mathbf{p}\|)$ to correct for differences between the near-field and far-field gains. Otherwise set $\alpha(\|\mathbf{p}\|) = 1$.
4) Calculate the PD matrix $\mathbf{R}_{\mathsf{PD}}(\mathbf{p})$ as

$$\mathbf{R}_{\mathsf{PD}}(\mathbf{p}) = \frac{P\alpha(\|\mathbf{p}\|)}{4\pi\|\mathbf{p}\|^2}\mathbf{M}^H\mathbf{a}(\mathbf{p})\mathbf{a}^H(\mathbf{p})\mathbf{M}. \tag{7}$$

Procedure for Computing Surface SAR Matrices: To compute the surface SAR matrix $\mathbf{R}_{\mathsf{SAR}_0}(\mathbf{p})$, follow the steps below:

1) Calculate the PD matrix $\mathbf{R}_{\mathsf{PD}}(\mathbf{p})$.
2) Determine angles of incidence (AoIs) ζ_n^i from the sources to the point $\mathbf{p}$ based on the tissue model.
3) Calculate the corresponding transmission coefficients τ_n assuming the incident wavefronts are plane waves, and define the diagonal $N \times N$ matrix $\mathbf{T}$ as

$$\mathbf{T} = \mathrm{diag}(\tau_0, \tau_1, \ldots, \tau_{N-1}). \tag{8}$$

For TE and TM polarized radiation, τ_n is given as

$$\begin{aligned}\tau_{n,\mathsf{TE}} &= \frac{2\cos\zeta_n^i}{\cos\zeta_n^i + \sqrt{\epsilon^* - \sin^2\zeta_n^i}},\\ \tau_{n,\mathsf{TM}} &= \frac{2\sqrt{\epsilon^*}\cos\zeta_n^i}{\epsilon^*\cos\zeta_n^i + \sqrt{\epsilon^* - \sin^2\zeta_n^i}}.\end{aligned} \tag{9}$$

4) Calculate the surface SAR matrix as

$$\mathbf{R}_{\mathsf{SAR}_0}(\mathbf{p}) = \frac{\eta_0\sigma}{\rho}\mathbf{T}^H\mathbf{R}_{\mathsf{PD}}(\mathbf{p})\mathbf{T}, \tag{10}$$

where η_0 is the intrinsic impedance of free space given by 377 Ω. Note that the tissue conductivity σ can be calculated from $\epsilon^* = \epsilon' - j\epsilon''$ as

$$\sigma = \omega\epsilon_0\epsilon'', \tag{11}$$

where ω is the transmission angular frequency and ϵ_0 is the permittivity of free space given by 8.85×10^{-12} F/m.

Apart from ϵ^*, all of the non-calculated parameters involved in these procedures are related to the transmitter and can be easily obtained from standard array measurements/simulations. Tissue permittivity measurements in the millimeter band are sparse due to technical limitations, but some studies have addressed models for human skin complex permittivity at millimeter wave frequencies [42]–[45]. Note that the measured parameters do not depend on the location of the user relative to the transmitter. Therefore, exposure matrices for various operating conditions can be computed with the same set of parameters.

III. MILLIMETER WAVE EXPOSURE MODELING

In this section, we derive the formulas for calculating exposure matrices provided in Section II-B. The problem of modeling pointwise incident PD and surface SAR is equivalent to estimating the incident and transmitted electric field across the body surface. Therefore, our objective is to approximate the near-field array pattern and the transmission of energy through the air-tissue boundary.

A. Incident Power Density

PD measurements are typically estimated by converting field strength measurements to plane wave equivalent PDs, and can be calculated as

$$S(\mathbf{p}) = \frac{\left|\mathcal{E}_m(\mathbf{p})\right|^2}{2\eta_0} = \frac{\left|\mathcal{H}_m(\mathbf{p})\right|^2}{2}\eta_0, \tag{12}$$

where $\mathcal{E}_m(\mathbf{p})$ is the electric field strength, $\mathcal{H}_m(\mathbf{p})$ is the magnetic field strength. Throughout this paper, it is assumed that PD refers to plane wave equivalent PD. Incident PD limits are often referred to as maximum permissible exposures (MPEs) in regulatory standards [18]. We derive an expression to compute the incident PD matrix $\mathbf{R}_{\mathsf{PD}}(\mathbf{p})$ for the quadratic model

$$S(\mathbf{p}, \mathbf{x}) = \mathbf{x}^H\mathbf{R}_{\mathsf{PD}}(\mathbf{p})\mathbf{x} \tag{13}$$

at a point $\mathbf{p}$ located near the transmitter array.

Since incident PD is proportional to $\left|\mathcal{E}_m(\mathbf{p})\right|^2$, calculating PD matrices requires minimal work if the variations in the transmitter array's radiated electric field as a function of $\mathbf{p}$ and $\mathbf{x}$ are known. However, this information is not always readily available and can be difficult to measure. Therefore, we focus on a more practical scenario in which only the far-field gain patterns of the antenna elements are known. The initial assumptions for the model development are as follows:

(A1) $\mathbf{p}$ is in the far-field of the antenna elements.
(A2) the antenna elements in the array are uncoupled.

Far-field conditions are dependent on the transmission wavelength λ and the array size. The general conditions for (A1) to hold are $\|\mathbf{p}\| > 2W_{\mathsf{max}}^2/\lambda$, $\|\mathbf{p}\| \gg W_{\mathsf{max}}$, and $\|\mathbf{p}\| \gg \lambda$, where W_{max} is the maximum linear dimension of the antenna elements. Some cases where (A2) holds include arrays with inter-element spacing that is large relative to λ and arrays fed by decoupling networks.

Incident PD at a point $\mathbf{p}$ can be expressed in terms of array parameters as

$$S(\mathbf{p},\mathbf{x}) = \frac{PG(\mathbf{p},\mathbf{x})}{4\pi\|\mathbf{p}\|^2}, \tag{14}$$

where P is the transmit power and $G(\mathbf{p},\mathbf{x})$ is the array gain. In cases where (A1) and (A2) hold, the far-field array gain is given by the principle of pattern multiplication [46]. Here, we use this principle to approximate the near-field array gain as

$$G(\mathbf{p},\mathbf{x}) \approx \left|\mathbf{a}^H(\mathbf{p})\mathbf{x}\right|^2, \tag{15}$$

where $\mathbf{a}(\mathbf{p})$ is the length N transmitter steering vector and $\mathbf{x}$ is the unit-norm length N transmit signal. The term $\mathbf{a}^H(\mathbf{p})\mathbf{x}$ is often referred to as the array factor. Note that (15) is an approximation because it assumes that the electric field vectors radiated by the antennas are roughly aligned, which may not hold at certain points near the array. This assumption is needed since we only know the far-field antenna gain patterns.

Steering vectors typically represent the set of phase delay differences corresponding to the radiated fields from each source and ignore path loss differences between wavefronts. This is only applicable far from the array, as the path lengths from each transmitter element to $\mathbf{p}$ may differ significantly when the point of interest is close to the array. These path length variations result in non-negligible attenuation differences between the waves which must be accounted for to calculate the array gain at $\mathbf{p}$. The steering vector is therefore constructed to represent the relative amplitudes and phase delays differences between spherical wavefronts as they impinge on $\mathbf{p}$ and is therefore defined as in (4). Note that $\mathbf{a}(\mathbf{p})$ is given in a general form that adapts to both the array geometry and the elements' gain patterns.

A characteristic matrix $\mathbf{R}_{\mathsf{PD}}(\mathbf{p})$ for the quadratic model of ideal PD can be defined using the expressions above as

$$\mathbf{R}_{\mathsf{PD,ideal}}(\mathbf{p}) \triangleq \frac{P}{4\pi\|\mathbf{p}\|^2}\mathbf{a}(\mathbf{p})\mathbf{a}^H(\mathbf{p}). \tag{16}$$

The matrix $\mathbf{R}_{\mathsf{PD,ideal}}(\mathbf{p})$ is a Hermitian, positive semi-definite matrix by construction. Note that the dominant eigenvector of the ideal PD matrix is a scalar multiple of the near-field array steering vector $\mathbf{a}(\mathbf{p})$, and maximum exposure occurs when $\mathbf{x}$ is aligned with $\mathbf{a}(\mathbf{p})$. This agrees with the intuition that plane wave equivalent PD is directly proportional to the array gain.

The characteristic matrix given in (16) is accurate under (A1) and (A2), but many exposure scenarios do not fall under these assumptions. Both near-field field components and mutual coupling can significantly affect array patterns and radiation emissions. We add correction factors to (16) to address both of these issues.

The near-field region of an array is characterized by complex field components that decrease with distance faster than $1/\|\mathbf{p}\|$. This results in gain patterns whose shape can vary significantly with distance from the source. In antenna measurement procedures where far-field conditions cannot be met, a gain pattern $G_{\mathsf{nf}}(\mathbf{p})$ is measured in the near-field and the far-field gain pattern is approximated from the model

$$G_{\mathsf{ff}}(\theta,\phi) \approx \alpha^{-1}(\|\mathbf{p}\|)G_{\mathsf{nf}}(\mathbf{p}), \tag{17}$$

where θ and ϕ are the elevation and azimuth angles of $\mathbf{p}$, respectively, and $\alpha(\|\mathbf{p}\|) \in \mathbb{R}_{>0}$ is the near-field gain correction factor (NFGCF) [47]. This only gives an estimate for the far-field gain since the NFGCF only varies with distance, but the error between the near-field and far-field gain patterns may have a directional dependence. The near-field gain converges to the far-field gain at large distances, therefore $\lim_{\|\mathbf{p}\|\to\infty}\alpha(\|\mathbf{p}\|) = 1$. The NFGCF can be estimated empirically by comparing measured data with theoretical gain curves that decay as $1/\|\mathbf{p}\|^2$ [47].

Array elements are often mutually coupled and act as parasitic elements that absorb and reradiate outgoing waves. A popular and simple method for modeling the field pattern of a coupled array is through an $N \times N$ coupling matrix $\mathbf{M}$ [48]–[50]. Let $\{\boldsymbol{\mathcal{E}}_{n,\mathsf{uc}}(\mathbf{p})\}_{n=0}^{N-1}$ denote the uncoupled three-dimensional electric field pattern of the array elements obtained from a unit excitation. The coupled array field pattern can be found as

$$\boldsymbol{\mathcal{E}}_{\mathsf{c}}(\mathbf{p}) = \boldsymbol{\mathcal{E}}_{\mathsf{uc}}(\mathbf{p})\mathbf{M}\mathbf{x}, \tag{18}$$

where $\boldsymbol{\mathcal{E}}_{\mathsf{uc}} = [\boldsymbol{\mathcal{E}}_{0,\mathsf{uc}}, \ldots \boldsymbol{\mathcal{E}}_{N-1,\mathsf{uc}}]$. In general, the coupling matrix cannot be determined exactly and must be estimated as in [48], [49]. Additionally, the coupling matrix $\mathbf{M}$ may vary depending on $\mathbf{p}$. However, we assume that $\mathbf{M}$ remains relatively constant over the exposed region of interest.

Incident PD Model: With the above models for ideal PD, near-field gain, and mutual coupling, the corrected characteristic exposure matrix to compute incident PD as $\mathbf{x}^H\mathbf{R}(\mathbf{p})\mathbf{x}$ is defined as

$$\begin{aligned}\mathbf{R}_{\mathsf{PD}}(\mathbf{p}) &\triangleq \alpha(\|\mathbf{p}\|)\mathbf{M}^H\mathbf{R}_{\mathsf{PD,ideal}}(\mathbf{p})\mathbf{M} \\ &= \frac{P\alpha(\|\mathbf{p}\|)}{4\pi\|\mathbf{p}\|^2}\mathbf{M}^H\mathbf{a}(\mathbf{p})\mathbf{a}^H(\mathbf{p})\mathbf{M},\end{aligned}$$

which is (7). The corrected matrix better approximates incident power density in non-ideal scenarios as shown in Section IV-B. It can also be seen that the corrected and uncorrected models agree under (A1) and (A2) since $\mathbf{R}_{\mathsf{PD}}(\mathbf{p}) = \mathbf{R}_{\mathsf{PD,ideal}}(\mathbf{p})$ when $\alpha(\|\mathbf{p}\|) = 1$ and $\mathbf{M} = \mathbf{I}$. The model in (7) is able to predict pointwise exposure with only prior knowledge of array parameters which are typically measured during the transmitter design. Note that the model not only predicts PD as a function of the transmit signal, but also as a function of space.

It can be seen that the PD matrix is rank-one by construction, and therefore it can be expressed as the outer product of its dominant eigenvector as $\mathbf{R}_{\mathsf{PD}}(\mathbf{p}) = \mathbf{r}(\mathbf{p})\mathbf{r}^H(\mathbf{p})$. In the ideal PD model, this eigenvector is colinear with the array steering vector $\mathbf{a}(\mathbf{p})$, whereas the coupling matrix and NFGCF rotate and scale the $\mathbf{a}(\mathbf{p})$ in the non-ideal scenario. In both cases, maximum exposure occurs when the transmit signal is aligned with the dominant eigenvector of the PD matrix, which can be expressed as a linear transformation of $\mathbf{a}(\mathbf{p})$. This motivates the notion of an *effective array steering vector* for a given exposure measure, which is defined as the vector $\hat{\mathbf{a}}_{\mathsf{EXP}}(\mathbf{p})$ such that

$$\mathsf{EXP}(\mathbf{p},\mathbf{x}) = \frac{\left|\hat{\mathbf{a}}^H(\mathbf{p})\mathbf{x}\right|^2}{\|\mathbf{p}\|^2}. \tag{19}$$

Note that for the proposed PD matrix, the effective array steering vector is given as

$$\hat{\mathbf{a}}_{\mathsf{PD}}(\mathbf{p}) = \sqrt{\frac{P\alpha(\|\mathbf{p}\|)}{4\pi}}\mathbf{M}^H\mathbf{a}(\mathbf{p}), \tag{20}$$

and so incident PD can be defined as the rank-one model

$$S(\mathbf{p},\mathbf{x}) = \frac{\left|\hat{\mathbf{a}}_{\mathsf{PD}}^H(\mathbf{p})\mathbf{x}\right|^2}{\|\mathbf{p}\|^2}. \tag{21}$$

PD calculations are relatively easy to perform for compliance, but they do not contain information about energy absorption in tissues. Incident electromagnetic waves are partially reflected when incident on dielectric media, which leads to significant differences in absorption for oblique incidence versus tangent incidence. Because of this, we consider SAR at the tissue surface as an alternative measurement for radiation absorption.

B. Specific Absorption Rate

Unlike incident PD, SAR must be measured, not calculated, with the device operating in its intended manner at full transmit power. Current methodologies require measuring SAR levels in a phantom head while the wireless device is held in a variety of operating conditions. Although current averaging volumes for SAR may not yield measurements that are useful for determining compliance in millimeter wave systems, SAR values at the tissue surface may serve as a suitable measure of energy deposition.

For a plane wave with power density $S(\mathbf{p},\mathbf{x})$ incident on a point $\mathbf{p}$ on the surface of planar tissue, the pointwise surface SAR, denoted as SAR_0 is given as

$$\text{SAR}_0(\mathbf{p},\mathbf{x}) = \frac{2TS(\mathbf{p},\mathbf{x})\cos\zeta^i}{\rho\delta}, \tag{22}$$

where T is the power transmission coefficient of the skin, ζ^i is the angle of incidence (AoI), and δ is the skin depth [42]. The skin depth is defined as the distance that electromagnetic radiation travels into a material before its power decreases to $\exp(-2)$ of its surface value and is given by

$$\delta = \frac{\lambda}{-2\pi\text{Im}(\sqrt{\epsilon^*})}, \tag{23}$$

where ϵ^* is the complex dielectric constant of the tissue [51]. Small penetration depths also lead to radiation absorption in tissue decreasing exponentially from the skin as

$$\text{SAR}(\mathbf{p},\mathbf{x},\xi) = \text{SAR}_0(\mathbf{p},\mathbf{x})e^{-2\xi/\delta}, \tag{24}$$

where ξ is the depth from the tissue surface [42]. Maximum exposure occurs at the surface of the tissue and quickly decays within the skin.

The expression in (22) is heavily dependent on the AoI ζ^i. Far from the array, this can approximated as the AoI from the center of the array to $\mathbf{p}$ because all path lengths $\|\mathbf{p}_n\|$ are approximately the same. We denote the surface SAR model in (22) with ζ^i calculated in this manner as the single plane wave (SPW) SAR model, since the incident radiation at $\mathbf{p}$ is assumed to be a plane wave with power density $S(\mathbf{p},\mathbf{x})$.

The approximations of the SPW model may lead to poor SAR estimates when $\mathbf{p}$ is close to the array. For example, if $\mathbf{p}$ is much closer to one of the array elements than to any other antenna, then ζ^i cannot be estimated as above. Moreover, the assumption that the incident wavefront behaves like a plane wave may not hold in general. Rather than computing surface SAR by finding the incident field at $\mathbf{p}$, we propose finding the total transmitted field as a superposition of the transmitted fields from each source.

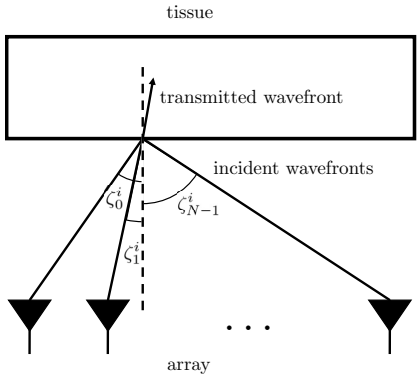

Fig. 2. Diagram of the considered electromagnetic radiation transmission scenario with array elements located near a planar tissue model. The radiated field from the n-th source impinges on the tissue surface at an angle of incidene ζ_n^i and contributes to the total transmitted field.

Consider the scenario in Fig. 2, where the transmitter array is a short distance away from a planar tissue surface. We assume all electromagnetic fields involved are time-harmonic and can therefore be represented in phasor form. For the n-th source, let ζ_n^i be the AoI of the incident wavefront and $\mathcal{E}_n^i(\mathbf{p})$ be the complex complex magnitude of the incident electric field at point $\mathbf{p}$. The transmitted electric field amplitudes can be expressed in terms of the incident field amplitudes and transmission coefficients τ_n as

$$\mathcal{E}_n^t(\mathbf{p}) = \tau_n\mathcal{E}_n^i(\mathbf{p}), \tag{25}$$

where the superscript t denotes the transmitted portion of the electric field. The total transmitted field can then be found as the sum of the individual fields as $\mathcal{E}^t(\mathbf{p}) = \sum_{n=0}^{N-1}\tau_n\mathcal{E}_n^i(\mathbf{p})$. Transmission coefficients are dependent on the field polarization, the shape of the incident waves, and the geometry of plane of incidence. Here, we assume that the incident waves and surface of incidence are planar. In this case, the transmission coefficients for TE and TM polarization are given as in (9).

Surface SAR Model: Since SAR is proportional to $\left|\mathcal{E}^t\right|^2$ and incident PD is proportional to $\left|\mathcal{E}^i\right|^2$, the surface SAR matrix is defined in terms of the PD model as

$$\mathbf{R}_{\mathsf{SAR}_0}(\mathbf{p}) \triangleq \frac{\eta_0\sigma}{\rho}\mathbf{T}^H\mathbf{R}_{\mathsf{PD}}(\mathbf{p})\mathbf{T},$$

which is (10), where $\mathbf{T}$ is a diagonal matrix with the transmission coefficients $\tau_0, \tau_1, \ldots, \tau_{N-1}$ in its diagonal. This SAR matrix can then be used to predict surface SAR at a point $\mathbf{p}$ as $\mathbf{x}^H\mathbf{R}_{\mathsf{SAR}_0}(\mathbf{p})\mathbf{x}$. Furthermore, the exponential decay model in (24) indicates that reducing average SAR measurements in

$$\mathbf{M}^{(2)} = \begin{bmatrix} 0.69+j0.03 & 0.07+j0.13 \\ 0.07+j0.13 & 0.69+j0.03 \end{bmatrix}, \mathbf{M}^{(4)} = \begin{bmatrix} 0.48+j0.03 & 0.06+j0.08 & -0.03-j0.03 & 0.02+j0.02 \\ 0.06+j0.08 & 0.47+j0.04 & 0.05+j0.08 & -0.03-j0.03 \\ -0.03-j0.03 & 0.06+j0.08 & 0.47+j0.04 & 0.05+j0.08 \\ 0.02+j0.02 & -0.03-j0.03 & 0.05+j0.08 & 0.48+j0.03 \end{bmatrix} \quad (26)$$

millimeter wave systems can be simplified to reducing surface SAR measurements. Note that $\mathbf{R}_{\mathsf{PD}}$ is calculated with the proposed PD model as in (7), so the proposed surface SAR model is valid even when (A1) and (A2) do not apply. It can be seen that the SAR matrix is also characterized by an effective array steering vector, given as

$$\hat{\mathbf{a}}_{\mathsf{SAR}}(\mathbf{p}) = \frac{\eta_0 \sigma}{\rho} \mathbf{T}^H \hat{\mathbf{a}}_{\mathsf{PD}}(\mathbf{p}), \quad (27)$$

and surface SAR can be modeled as

$$\mathsf{SAR}_0(\mathbf{p}, \mathbf{x}) = \frac{\left|\hat{\mathbf{a}}_{\mathsf{SAR}}^H(\mathbf{p})\mathbf{x}\right|^2}{\|\mathbf{p}\|^2}. \quad (28)$$

In this case, the rotation of the steering vector is dependent on $\mathbf{p}$ through $\mathbf{T}$.

IV. Model Verification Results

In this section, we validate the proposed formulas for exposure matrices in (7) and (10) by simulating a simple millimeter wave exposure scenario in ANSYS High Frequency Structure Simulator (HFSS) software. The following examples demonstrate that the quadratic signal-level models can predict exposure values from software simulations with high accuracy, even in non-ideal settings.

A. Dipole Array Parameters and Head Model

We consider N element uniform linear arrays (ULAs) of half-wavelength dipoles placed on the x-axis transmitting at 28 GHz. In all simulations, the inter-element spacing of the array is $\lambda/2$ and the system transmit power P is 10 mW. Simulations were performed with both ideal and non-ideal dipoles. The use of ideal dipoles indicates that the antennas were implemented as cylindrical sources with the theoretical radiation pattern of a linear antenna in both the near-field and the far-field. Note that simulations with ideal dipoles fall under (A1) and (A2). Non-ideal dipoles were also modeled in HFSS in order to validate the proposed models in the presence of mutual coupling and near-field effects.

The parameters for the ideal and non-ideal dipoles are shown in Table II. At the operating frequency of 28 GHz, the ideal and non-ideal dipoles achieved a maximum gain of 1.64 and 1.76, respectively, in the xy-plane. For simplicity, all exposure testing points in the validation results are assumed to lie in the xy-plane. The coupling matrices were calculated with the array Z-parameters as described in [48]. This resulted in the normalized coupling matrices $\mathbf{M}^{(2)}$ and $\mathbf{M}^{(4)}$ shown in (26), for a two-element and four-element ULA, respectively. The NFGCFs were obtained by comparing the predicted and actual array gain at a point 5 mm away from the transmitter at boresight, giving the factors $\alpha^{(2)} = 1.43$ and $\alpha^{(4)} = 2.91$ for arrays of two and four elements, respectively.

TABLE II
Dipole antenna parameter specifications.

Parameter	Specifications	
	Ideal Dipole	Non-ideal Dipole
Total Length (mm)	5.353	5.065
Radius (mm)	0.01	0.01
Source Length (mm)	N/A	0.05
Source Impedance (Ω)	N/A	71.18

For SAR simulations, we consider a hemispherical head model with a 20 mm radius centered on the y-axis at a point 5 mm away from the origin, as seen in Fig. 3. The head tissue is assumed to be homogeneous with complex dielectric constant $\epsilon^* = 19 - j19.26$ approximately based on Gandhi's model in [42] at a frequency of 28 GHz, giving a tissue conductivity of $\sigma = 30$ S/m. The tissue density is assumed to be 1 g/cm^3. SAR values in HFSS were obtained at a depth of 0.2 mm.

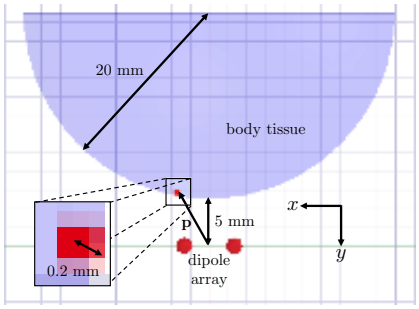

Fig. 3. HFSS setup for SAR simulations. The dipole array is placed 5 mm away from a hemispherical tissue model with radius 20 mm, complex dielectric constant $\epsilon^* = 19 - j19.26$, and tissue density 1 g/cm^3. SAR values are obtained at a depth of 0.2 mm from the surface point $\mathbf{p}$.

Since the SAR simulation results were obtained below the tissue surface, we scale the proposed SAR model and SPW model by a constant β to properly account for absorption losses. To determine β, we simulated a plane wave traveling in the $-y$ direction and measured pointwise SAR on the y-axis at a depth of 0.2 mm below the tissue surface. This SAR reading was compared to the predicted surface SAR value obtained from (22) to compute β. For the head model with parameters as discussed above, this procedure resulted in a scaling coefficient $\beta = 0.7024$. The same scaling coefficient was used for all SAR scenarios.

B. Incident PD Model Validation

In the first example, we compare incident PD values obtained from simulations to the quadratic PD model. A beam

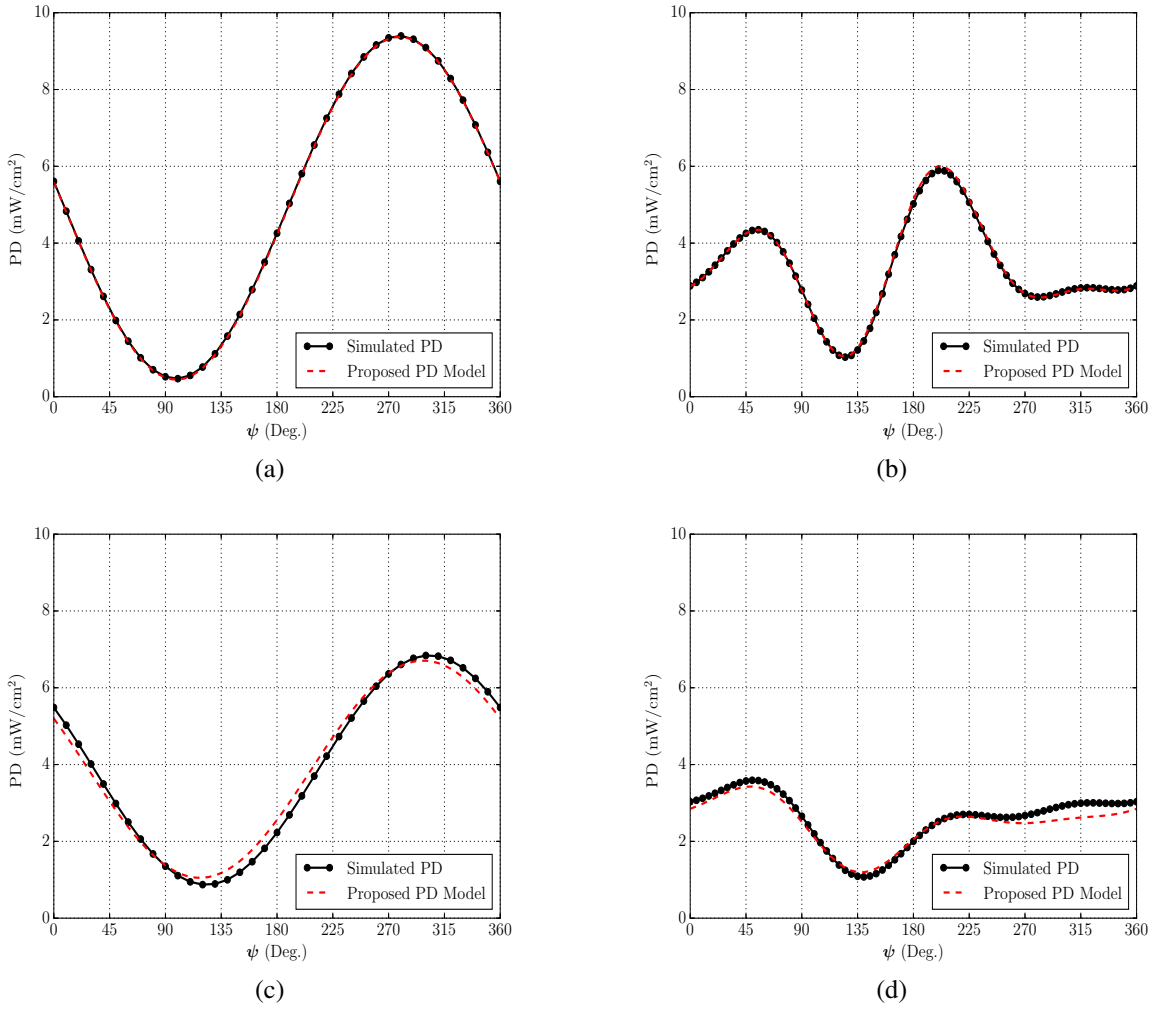

Fig. 4. Plane wave equivalent PD values from HFSS simulations and the quadratic model $\mathbf{x}^H\mathbf{R}_{\mathsf{PD}}(\mathbf{p})\mathbf{x}$, with PD matrices calculated as in (7), vs. the beam sweep angle ψ of the transmit signal $\mathbf{x}$ in (29). The point $\mathbf{p}$ is located 5 mm from the array center and at 30° from boresight. Results with half-wave dipole ULAs are shown in the ideal case with (a) $N = 2$ and (b) $N = 4$, and in the non-ideal case with $N = 2$ and $N = 4$ in (c) and (d), respectively. The dipole antenna parameters are given in Table II, and the array coupling matrices are given in (26).

sweep is performed by setting the transmit signal as

$$\mathbf{x} = \frac{1}{\sqrt{N}}\left[1,\, e^{j\psi},\, e^{j2\psi},\, \ldots,\, e^{j(N-1)\psi}\right]^{\mathsf{T}}, \qquad (29)$$

and varying ψ. Plane wave equivalent PD values were obtained from HFSS at a point $\mathbf{p}$ located 5 mm from the center of the array at 30° from boresight. These results were compared to the PD model $\mathbf{x}^H\mathbf{R}_{\mathsf{PD}}\mathbf{x}$ for various values of ψ. The PD matrices were calculated in terms of the simulation parameters and the point $\mathbf{p}$ using (7). For example, the matrix for a two-element ULA with ideal dipoles was computed as

$$\mathbf{R}_{\mathsf{PD}}^{(2)} = \begin{bmatrix} 2.87 & 0.68 + j4.41 \\ 0.68 - j4.41 & 6.95 \end{bmatrix}. \qquad (30)$$

Fig. 4 (a) and (b) demonstrate a high agreement between the proposed PD model and the simulation results in the ideal case. The PD model also demonstrates high accuracy in estimating the simulated exposure values in a non-ideal scenario as seen in Fig. 4 (c) and (d). Note that in both the ideal and non-ideal cases, the error between the model and the simulated values may be larger in cases where $\mathbf{p}$ is far from the xy-plane but is still relatively close to the array since the radiated electric field vectors from the antenna elements may be misaligned. However, these points will in general experience lower exposure than points in the xy-plane due to the dipole gain patterns, and therefore are of less importance.

C. Surface SAR Model Validation

In the second example, we consider the surface point $\mathbf{p} = [3.47, -5.30, 0]^T$ mm on the head model in Fig. 3. Fig. 5 shows the comparison between simulated measurements from HFSS and both the SPW SAR model and the proposed SAR model $\mathbf{x}^H\mathbf{R}_{\mathsf{SAR}}(\mathbf{p})\mathbf{x}$ with $\mathbf{R}_{\mathsf{SAR}}(\mathbf{p})$ found as in (10). For example, the scaled SAR matrix $\beta\mathbf{R}_{\mathsf{SAR}}(\mathbf{p})$ for a two-element ULA with ideal dipoles was determined to be

$$\mathbf{R}_{\mathsf{SAR}}^{(2)} = \begin{bmatrix} 5.20 & -0.20 + j13.49 \\ -0.20 - j13.49 & 35.04 \end{bmatrix}. \qquad (31)$$

In the non-ideal case, we found an error between the amplitude of the proposed model and the simulated SAR even when

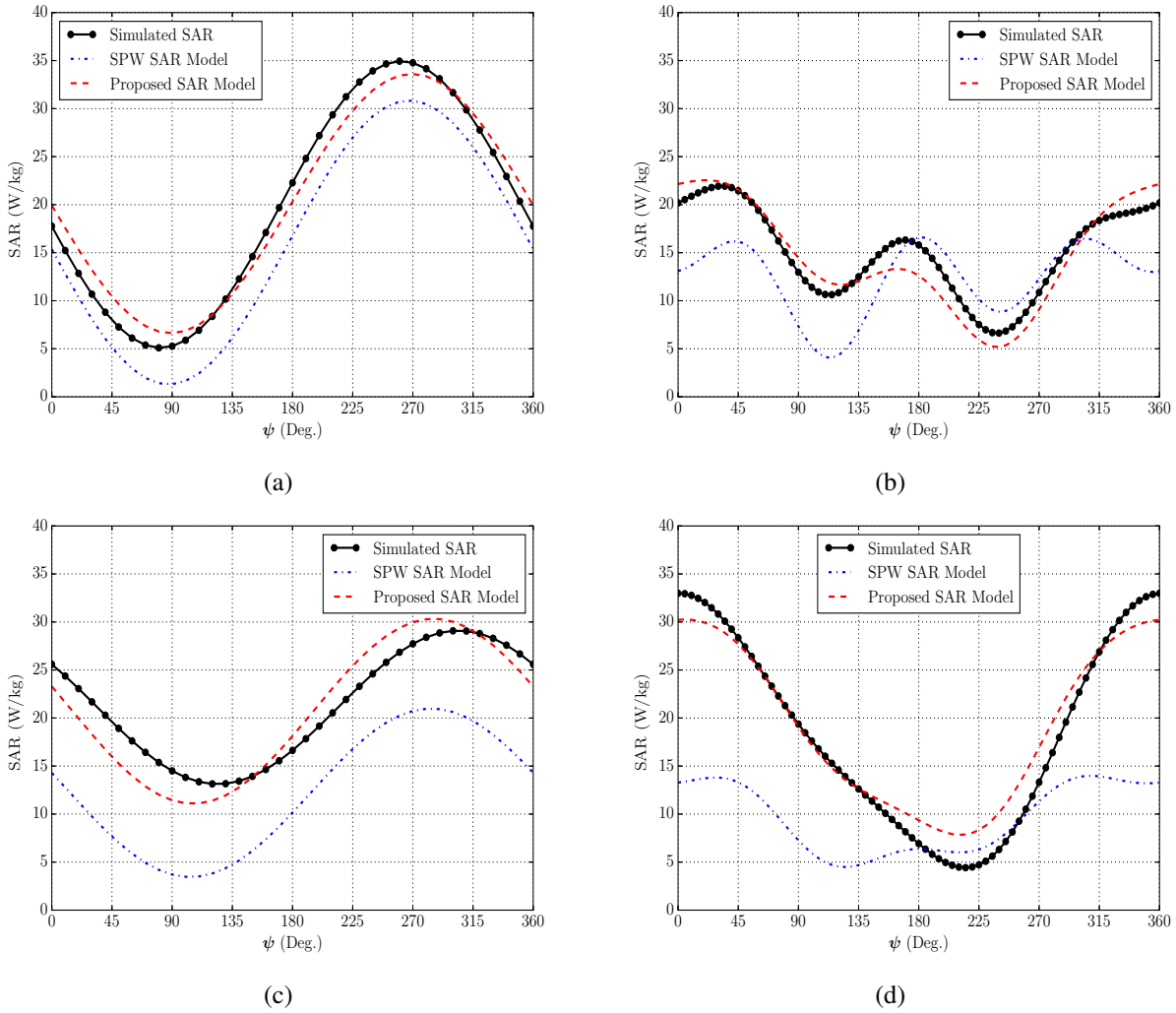

Fig. 5. SAR values from HFSS simulations, the SPW SAR model in (22), and the quadratic model $\mathbf{x}^H \mathbf{R}_{\mathsf{SAR}}(\mathbf{p})\mathbf{x}$, with SAR matrices calculated as in (10), vs. the beam sweep angle ψ of the transmit signal $\mathbf{x}$ in (29). The exposure scenario is shown in Fig. 3. Non-simulated values were scaled by a factor of 0.7024 to account for absorption losses. Results with half-wave dipole ULAs are shown in the ideal case with (a) $N = 2$ and (b) $N = 4$, and in the non-ideal case with $N = 2$ and $N = 4$ in (c) and (d), respectively. The dipole antenna parameters are given in Table II, and the array coupling matrices are given in (26). In the non-ideal cases, the proposed model was scaled by a factor of $K = 1.203$ and $K = 1.423$ in (c) and (d), respectively.

taking the absorption coefficient into consideration. These discrepancies could be caused by a variety of unaccounted factors, such as coupling between the antennas and the head model, the curvature of the head model, and the depth at which SAR is simulated. To address this issue, the predicted SAR values were scaled by a constant K, which was chosen to minimize the error between the proposed model and the simulated values. We note that this scaling constant was only used in the case of the non-ideal dipoles.

The results demonstrate that the proposed model can predict the simulated SAR values with high accuracy. More importantly, the shape of the curves produced by the proposed model closely match that of the simulation results, especially compared to the SPW model curves. This suggests that the model can predict which transmit signals result in relatively high and low exposure values. Therefore, the model can still be applied to design transmission schemes which minimize exposure levels even if K cannot be determined accurately. In addition, any amplitude offset between the proposed model and actual SAR measurements can be lumped into the effective transmit power of the device and controlled through power control settings.

V. Exposure Model Analysis and Applications

Given a wireless device and a model for the exposed body, the proposed models for incident PD and surface SAR enable systems to estimate pointwise exposure over regions in space. Let $\mathcal{P}$ be a set of testing points or a region over which exposure is regulated, such as a superficial area on a head model or a region surrounding the transmitter array. Then an exposure constraint over $\mathcal{P}$ can be expressed as

$$\mathsf{EXP}(\mathbf{p}, \mathbf{x}) \leq Q, \, \forall \mathbf{p} \in \mathcal{P}, \tag{32}$$

where Q is the regulatory exposure threshold. However, if $\mathcal{P}$ is defined as a contiguous area or volume, it is unfeasible to directly incorporate this constraint into signal design algorithms to mitigate electromagnetic absorption. In this section,

we present methods for sampling $\mathcal{P}$ in order to characterize exposure over the entire testing region within a certain error threshold with a finite number of points. We then leverage this sampled representation to obtain a method for calculating exposure matrices for predicting average exposure, rather than pointwise exposure.

A. Sampling Methods

Let $\mathbf{p}$ and $\tilde{\mathbf{p}}$ be two points in the region $\mathcal{P}$. We first examine the relationship between the maximum difference in exposure levels at these points, given as

$$d_{\mathsf{EXP}}(\mathbf{p},\tilde{\mathbf{p}}) = \max_{\mathbf{x}:\|\mathbf{x}\|=1} \left|\mathsf{EXP}(\mathbf{p},\mathbf{x}) - \mathsf{EXP}(\tilde{\mathbf{p}},\mathbf{x})\right|, \tag{33}$$

and inter-point distance $\|\mathbf{p}-\tilde{\mathbf{p}}\|$.

Note that the highest levels of exposure occur at points which are closest to the array and which lie in the direction of the highest array gain. These characteristics can be captured by the minimum distance to the array over $\mathcal{P}$, denoted as r_{min}, and the maximum directivity over $\mathcal{P}$ among the antennas, denoted as G_{max}. The minimum distance r_{min} is defined as the smallest distance from a point in $\mathcal{P}$ to any antenna element and is given as

$$r_{\mathsf{min}} = \min_{\mathbf{p}\in\mathcal{P}} r_{\mathsf{min}}(\mathbf{p}), \tag{34}$$

where $r_{\mathsf{min}}(\mathbf{p})$ is smallest distance to $\mathbf{p}$ over the array elements,

$$r_{\mathsf{min}}(\mathbf{p}) = \min_{n=0,1,\ldots,N-1} \|\mathbf{p}_n\|. \tag{35}$$

Likewise, the maximum directivity G_{max} can be defined in terms of the individual gain patterns as

$$G_{\mathsf{max}} = \max_{n=0,1,\ldots,N-1} \max_{\mathbf{p}\in\mathcal{P}} g_n(\mathbf{p}_n). \tag{36}$$

These parameters correspond to a worst-case scenario in terms of exposure, and are therefore useful in bounding $d_{\mathsf{EXP}}(\mathbf{p},\tilde{\mathbf{p}})$.

We now state the following lemma as a preliminary step in characterizing an upper bound on $d_{\mathsf{EXP}}(\mathbf{p},\tilde{\mathbf{p}})$.

Lemma 1. *Let $\mathbf{p}$ and $\tilde{\mathbf{p}}$ be distinct points in a set $\mathcal{P}$ not containing the origin. Assume that $g_n(\mathbf{p}_n)$ is constant over $\mathcal{P}$. Then we have that for any non-zero transmit signal $\mathbf{x}$,*

$$\left|\frac{\left|\mathbf{a}^H(\mathbf{p})\mathbf{x}\right|^2}{\|\mathbf{p}\|^2} - \frac{\left|\mathbf{a}^H(\tilde{\mathbf{p}})\mathbf{x}\right|^2}{\|\tilde{\mathbf{p}}\|^2}\right| < \varepsilon \tag{37}$$

as long as $\|\mathbf{p}-\tilde{\mathbf{p}}\| < \Delta/\|\mathbf{x}\|^2$, where Δ is given as

$$\Delta = \frac{\varepsilon r_{\mathsf{min}}^2}{2N^2 G_{\mathsf{max}}}\left(\frac{4\pi}{\lambda}+\frac{1}{r_{\mathsf{min}}}\right)^{-1}. \tag{38}$$

The proof is found in Appendix A. The constant gain assumption can be satisfied by choosing $\mathcal{P}$ to be sufficiently small.

Although Lemma 1 only bounds the difference in a quantity closely related to PD, the structure of the exposure models allow this result to be applied to both the PD and SAR models. As demonstrated in Section II, both PD and surface SAR matrices can be characterized by an steering vector, and exposure at $\mathbf{p}$ can be modeled as a rank-one quadratic as in (19). The effective steering vector $\hat{\mathbf{a}}_{\mathsf{EXP}}(\mathbf{p})$ can be expressed as a spatially dependent linear transformation on $\mathbf{a}(\mathbf{p})$ of the form

$$\hat{\mathbf{a}}_{\mathsf{EXP}}(\mathbf{p}) = k_{\mathsf{EXP}}\mathbf{D}(\mathbf{p})\mathbf{W}\mathbf{a}(\mathbf{p}), \tag{39}$$

where k_{EXP} is a constant of proportionality dependent on the exposure measure, $\mathbf{D}(\mathbf{p})$ is an $N\times N$ diagonal matrix defined as a function of $\mathbf{p}$, and $\mathbf{W}$ is a $N\times N$ matrix. For example, the PD effective steering vector $\hat{\mathbf{a}}_{\mathsf{PD}}(\mathbf{p})$ can be obtained by setting $k_{\mathsf{PD}} = \sqrt{P/4\pi}$, $\mathbf{D}(\mathbf{p}) = \alpha^{1/2}(\|\mathbf{p}\|)\mathbf{I}$ and $\mathbf{W} = \mathbf{M}^H$. For simplicity we assume that the region of interest is small enough so that $\mathbf{D}(\mathbf{p})$ can be approximated by a constant matrix $\mathbf{D}$ over $\mathcal{P}$.

The linear transformation in (39) and Lemma 1 can then be applied to show the following result.

Lemma 2. *Let $\mathbf{p}$ and $\tilde{\mathbf{p}}$ be distinct points in a set $\mathcal{P}$ not containing the origin. Assume that $g_n(\mathbf{p}_n)$ is constant over $\mathcal{P}$ and that $\mathbf{W}$ is full rank. Then*

$$d_{\mathsf{EXP}}(\mathbf{p},\tilde{\mathbf{p}}) < \varepsilon \tag{40}$$

as long as

$$\|\mathbf{p}-\tilde{\mathbf{p}}\| < \Delta_{\mathsf{EXP}} \triangleq \frac{\Delta}{k_{\mathsf{EXP}}^2\|\mathbf{W}\mathbf{D}\|_2^2}, \tag{41}$$

where Δ is given as in Lemma 1.

Proof: By substituting (19) into the definition of $d_{\mathsf{EXP}}(\mathbf{p},\tilde{\mathbf{p}})$, we have that

$$d_{\mathsf{EXP}}(\mathbf{p},\tilde{\mathbf{p}}) = \max_{\mathbf{x}:\|\mathbf{x}\|=1}\left|\frac{\left|\hat{\mathbf{a}}_{\mathsf{EXP}}^H(\mathbf{p})\mathbf{x}\right|^2}{\|\mathbf{p}\|^2} - \frac{\left|\hat{\mathbf{a}}_{\mathsf{EXP}}^H(\tilde{\mathbf{p}})\mathbf{x}\right|^2}{\|\tilde{\mathbf{p}}\|^2}\right|. \tag{42}$$

Since effective steering vectors in (42) are linear transformations of $\mathbf{a}(\mathbf{p})$, $d_{\mathsf{EXP}}(\mathbf{p},\tilde{\mathbf{p}})$ can be expressed as

$$d_{\mathsf{EXP}}(\mathbf{p},\tilde{\mathbf{p}}) = \max_{\mathbf{x}:\|\mathbf{x}\|=1}\left|\frac{\left|\mathbf{a}^H(\mathbf{p})\hat{\mathbf{x}}\right|^2}{\|\mathbf{p}\|^2} - \frac{\left|\mathbf{a}^H(\tilde{\mathbf{p}})\hat{\mathbf{x}}\right|^2}{\|\tilde{\mathbf{p}}\|^2}\right|, \tag{43}$$

where $\hat{\mathbf{x}}$ is the effective transmit signal given as

$$\hat{\mathbf{x}} = k_{\mathsf{EXP}}\mathbf{W}^H\mathbf{D}^H\mathbf{x}. \tag{44}$$

Applying Lemma 1 with the effective transmit signal $\hat{\mathbf{x}}$, we have that if

$$\|\mathbf{p}-\tilde{\mathbf{p}}\| < \frac{\Delta}{\max_{\mathbf{x}:\|\mathbf{x}\|=1}\|\hat{\mathbf{x}}\|^2} = \frac{\Delta}{k_{\mathsf{EXP}}^2\|\mathbf{D}\mathbf{W}\|_2^2}, \tag{45}$$

then $d_{\mathsf{EXP}}(\mathbf{p},\tilde{\mathbf{p}}) < \varepsilon$ as desired. ∎

The previous results not only imply that the maximum exposure differential $d_{\mathsf{EXP}}(\mathbf{p},\tilde{\mathbf{p}})$ can be guaranteed to lie below the error threshold ε if the two testing points are sufficiently close, but also give an explicit expression for the maximum allowable distance between the two points. The assumption that $\mathbf{W}$ is full rank, which is equivalent to $\mathbf{M}$ having full rank, corresponds with the notion that non-zero transmit signals cannot induce an eletric field of zero over $\mathcal{P}$ and is thus reasonable in the context of this study. These bounds are now applied to formulate uniform and non-uniform sampling methods which allow us to characterize pointwise exposure over $\mathcal{P}$ in terms of a finite number of points at the cost of a predetermined margin of error.

Uniform Sampling: A direct application of Lemma 2 yields a method for uniformly sampling the region $\mathcal{P}$. Let ε be the desired maximum exposure variation between adjacent points. Then sampling points in $\mathcal{P}$ at a maximum distance of Δ_{EXP} guarantees that the exposure differential between two adjacent points is at most ε. Note that this criteria only gives a guideline for the allowable distance between sample points, since the specific manner of sampling should be determined based on the body tissue geometry. However, we provide a numerical example in Section IV-C to demonstrate how to sample a relatively simple region.

Non-uniform Sampling: A shortcoming of the uniform sampling method is that it does not leverage the decay of electromagnetic field strengths with distance from sources. Intuitively, exposure values should follow a downward trend as points move farther from the transmitter and thus the distance between sampled points should be allowed to increase without penalty. This dependence can be seen in the term Δ_{EXP}, which increases with r_{min}^3. Additionally, other model parameters which are dependent on location, such as the transmission coefficients and the NFGCF, also affect the sampling distance. The uniform sampling approach restricts Δ_{EXP} to a constant value based on the point closest to the array, but a non-uniform method can be developed by adaptively adjusting the sampling distance.

The main idea of the non-uniform sampling algorithm is to sample the closest points to the array first and move outwards while adaptively adjusting the sampling distance. Given a spatial region $\mathcal{P}$, we first sample the closest point to the transmitter array, given as

$$\mathbf{p}_0 = \underset{\mathbf{p}\in\mathcal{P}}{\operatorname{argmin}}\, r_{\mathsf{min}}(\mathbf{p}). \tag{46}$$

Based on Lemmas 1 and 2, a positionally dependent sampling distance can be defined as

$$\Delta_{\mathsf{EXP}}(\mathbf{p}) \triangleq \frac{\varepsilon r_{\mathsf{min}}^2(\mathbf{p})}{2N^2 G_{\mathsf{max}} k_{\mathsf{EXP}}^2 \left\|\mathbf{WD}(\mathbf{p})\right\|_2^2} \times \left(\frac{4\pi}{\lambda} + \frac{1}{r_{\mathsf{min}}(\mathbf{p})}\right)^{-1}. \tag{47}$$

According to the uniform sampling criteria, the next sample points should be located at a distance of $\Delta_{\mathsf{EXP}}(\mathbf{p}_0)$ from $\mathbf{p}_0$. Let $\mathbf{p}_1$ be one of those points, and let $\Delta_{\mathsf{EXP}}(\mathbf{p}_1)$ be the sampling distance corresponding to $\mathbf{p}_1$. Since exposure at points closer to the array than $\mathbf{p}_1$ is characterized by the sample at $\mathbf{p}_0$, the remaining sample points will be located farther from the array than $\mathbf{p}_1$. Therefore, the next sample point, $\mathbf{p}_2$, is chosen to lie at a maximum distance of $\Delta_{\mathsf{EXP}}(\mathbf{p}_1)$ from $\mathbf{p}_1$, as doing so ensures that the conditions of Lemma 2 are still satisfied and the exposure differential between $\mathbf{p}_1$ and $\mathbf{p}_2$ is bounded as $d_{\mathsf{EXP}}(\mathbf{p}_1, \mathbf{p}_2) < \varepsilon$. This procedure is repeated until the entire region is sampled.

B. Spatially Averaged Exposure Model

As previously mentioned, regulation agencies measure spatially averaged exposure rather than pointwise exposure in order to determine whether wireless devices comply with exposure thresholds. The sampling methods developed in the previous section allow us to characterize modeled exposure over a region $\mathcal{P}$ with a finite number of points. We now show how this representation can be used to estimate spatially averaged exposure over $\mathcal{P}$, given as

$$\mathsf{EXP}_{\mathsf{avg}}(\mathcal{P}) = \frac{\int_{\mathcal{P}} \mathsf{EXP}(\mathbf{p}, \mathbf{x}) d\mathbf{p}}{|\mathcal{P}|}, \tag{48}$$

where $|\mathcal{P}|$ is the area or volume of $\mathcal{P}$, with a quadratic model $\mathbf{x}^H \mathbf{R}_{\mathsf{avg}}(\mathcal{P})\mathbf{x}$. For simplicity, we shortly drop the dependence of the exposure function on the transmit signal $\mathbf{x}$.

Let $\mathcal{P}$ be the region over which measurements are averaged and let

$$\mathcal{P}_{\mathsf{s}} = \left\{\mathbf{p}^{(0)}, \mathbf{p}^{(1)}, \ldots, \mathbf{p}^{(M-1)}\right\} \tag{49}$$

be the M sample points obtained by applying either of the proposed sampling methods on $\mathcal{P}$. The region $\mathcal{P}$ can be divided into subregions corresponding to each sample point as

$$\mathcal{P}^{(m)} = \left\{\mathbf{p} \in \mathcal{P} : \mathbf{p}^{(m)} = \underset{\tilde{\mathbf{p}}\in\mathcal{P}_{\mathsf{s}}}{\operatorname{argmin}} \|\mathbf{p} - \tilde{\mathbf{p}}\|\right\}. \tag{50}$$

The m-th subregion consists of the points in $\mathcal{P}$ lying closest to the m-th sample point, and these subregions define a partition of $\mathcal{P}$. Therefore, average exposure over $\mathcal{P}$ can be written as

$$\mathsf{EXP}_{\mathsf{avg}}(\mathcal{P}) = \frac{\sum_{m=0}^{M-1} \int_{\mathcal{P}^{(m)}} \mathsf{EXP}(\mathbf{p}) d\mathbf{p}}{|\mathcal{P}|}. \tag{51}$$

Assuming there are no discontinuities in the electromagnetic field over $\mathcal{P}$, the integral Mean Value Theorem gives us that the average exposure over each subregion $\mathcal{P}^{(m)}$ is equal to the exposure value at some point $\tilde{\mathbf{p}}^{(m)}$ in the subregion. This relationship can be formally stated as

$$\mathsf{EXP}(\tilde{\mathbf{p}}^{(m)}) = \frac{\int_{\mathcal{P}^{(m)}} \mathsf{EXP}(\mathbf{p}) d\mathbf{p}}{\left|\mathcal{P}^{(m)}\right|}. \tag{52}$$

Note that the point $\tilde{\mathbf{p}}^{(m)}$ belongs to the m-th sample point's subregion. Moreover, the distance between $\mathbf{p}_m$ and $\tilde{\mathbf{p}}_m$ must be less than the distance between $\mathbf{p}_m$ and its neighboring sample points. Thus, Lemma 2 ensures that

$$d_{\mathsf{EXP}}(\mathbf{p}_m, \tilde{\mathbf{p}}_m) < \varepsilon. \tag{53}$$

Combining the expressions (51) and (52) with the bound in (53), we have that average exposure over the entire region can be approximated as

$$\mathsf{EXP}_{\mathsf{avg}}(\mathcal{P}) \approx \frac{\sum_{m=0}^{M-1} \left|\mathcal{P}^{(m)}\right| \mathsf{EXP}(\mathbf{p}^{(m)})}{|\mathcal{P}|}. \tag{54}$$

If $\mathcal{P}$ is sampled such that each subregion is of the same size, average exposure can be approximated as the arithmetic mean of the sample points as

$$\mathsf{EXP}_{\mathsf{avg}}(\mathcal{P}) \approx \mathsf{EXP}_{\mathsf{avg}}(\mathcal{P}_{\mathsf{s}}) \triangleq \frac{1}{M} \sum_{m=0}^{M-1} \mathsf{EXP}(\mathbf{p}^{(m)}). \tag{55}$$

In this case, the maximum error between the approximation in (55) and the true averaged exposure, given as

$$d_{\mathsf{EXP}}(\mathcal{P}, \mathcal{P}_{\mathsf{s}}) = \max_{\mathbf{x}:\|\mathbf{x}\|=1} \left|\mathsf{EXP}_{\mathsf{avg}}(\mathcal{P}) - \mathsf{EXP}_{\mathsf{avg}}(\mathcal{P}_{\mathsf{s}})\right|, \tag{56}$$

will also be bounded by ε. The approximation for average exposure given in (55) can also be written in terms of the signal-level model as

$$\mathsf{EXP}_{\mathsf{avg}}(\mathcal{P}_{\mathsf{s}}, \mathbf{x}) = \frac{1}{M} \sum_{m=0}^{M-1} \mathbf{x}^H \mathbf{R}_{\mathsf{EXP}}(\mathbf{p}^{(m)}) \mathbf{x} \tag{57}$$

$$= \mathbf{x}^H \left(\frac{1}{M} \sum_{m=0}^{M-1} \mathbf{R}_{\mathsf{EXP}}(\mathbf{p}^{(m)}) \right) \mathbf{x} \tag{58}$$

$$\triangleq \mathbf{x}^H \mathbf{R}_{\mathsf{EXP,\,avg}}(\mathcal{P}) \mathbf{x}, \tag{59}$$

where the matrix $\mathbf{R}_{\mathsf{EXP,\,avg}}(\mathcal{P})$ now characterizes average exposure over $\mathcal{P}$. In general, the average exposure matrix can be written as a weighted average of the exposure matrices for each sample point as

$$\mathbf{R}_{\mathsf{EXP,\,avg}}(\mathcal{P}) = \frac{1}{|\mathcal{P}|} \sum_{m=0}^{M-1} \left| \mathcal{P}^{(m)} \right| \mathbf{R}_{\mathsf{EXP}}(\mathbf{p}^{(m)}). \tag{60}$$

In practice, average exposure matrices $\mathbf{R}_0, \mathbf{R}_1, \ldots, \mathbf{R}_{L-1}$ corresponding to L different body regions and/or gestures can be calculated offline to model exposure over a variety of operating conditions. A worst-case constraint on the system can then be defined as

$$\max_{\ell=0,1,\ldots,L-1} \mathbf{x}^H \mathbf{R}_\ell \mathbf{x} \leq Q. \tag{61}$$

This constraint is identical to those examined in [1], [30], [31], [36]–[39], therefore the signaling schemes developed in these studies can be applied to jointly maximize the far-field rate performance while controlling near-field exposure.

C. Numerical Examples of Sampling Methods

We present a numerical example to demonstrate the application of the proposed sampling guidelines. We consider a scenario similar to that in Fig. 3, but with a spherical head model with a radius of 90 mm at a distance d away from a transmitter equipped with N ideal half-wave dipoles operating at a frequency of 28 GHz. We assume an incident power density constraint is placed on the surface of the head model in the xy-plane, where maximum exposure occurs.

The surface of the head model was sampled for $N = 2$ and $d = 10$ mm according to the uniform and non-uniform sampling guidelines as seen in Fig. 6. For illustrative purposes, the transmit power was set to $P = 10$ mW and the variation threshold ε was set to 25 mW/cm^2. The sampled area corresponds to an arc of length 94.25 mm centered at boresight from the center of the transmitter. Note that although the uniform sampling forces points to be located in close proximity, the non-uniform approach allows sparser sampling at points relatively far from the transmitter. It takes 51 points to uniformly sample the region, whereas the region can be sampled with only 17 points using the non-uniform method.

The number of sample points required to sample the region from the previous example with a variation threshold of $\varepsilon = 1$ mW/cm^2 for various combinations of values for N and d are shown in Tables III. In all cases, non-uniform sampling requires a significantly smaller number of points than the uniform method but the sampling distance must be recalculated at each iteration, increasing the computational complexity of this approach. Although the amount of sampling required in all cases seems onerous, this is due to the restrictive bound we have placed on the maximum difference between *pointwise* exposure measurements. For practical applications, the sample points should be used to compute average exposure matrices as discussed in Section IV-B.

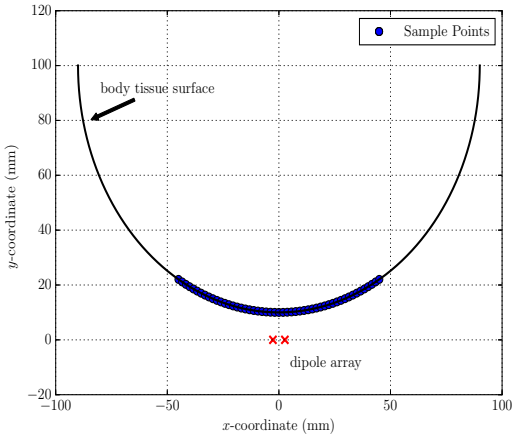

(a)

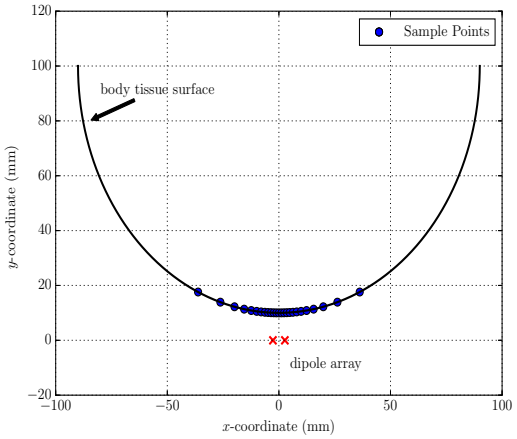

(b)

Fig. 6. Plots of the sampling points obtained from the (a) uniform and (b) non-uniform sampling approaches over the surface of a spherical head model with radius 90 mm at a distance of 10 mm from a two-element ideal dipole ULA. Sampling was performed with an error parameter of $\epsilon = 25$ mW/cm^2.

TABLE III
NUMBER OF SAMPLE POINTS FOR DIFFERENT CHOICES OF N AND d.

Parameters	# Sampling Points	
	Uniform	Non-uniform
$d = 10$ mm, $N = 2$	1251	343
$d = 10$ mm, $N = 4$	5003	1359
$d = 5$ mm, $N = 2$	5357	787
$d = 5$ mm, $N = 4$	21425	3133

D. Average Exposure Model Validation

In order to validate the average exposure model, we consider two arcs, denoted as $\mathcal{P}_1$ and $\mathcal{P}_2$, on the surface of a head model of radius $R = 90$ mm next to a 2-element dipole array at distance of $d = 5$ mm from the head, as shown in Fig. 7. These regions were sampled uniformly and non-uniformly according to the proposed guidelines. As in Section IV, we assume that the transmitter is equipped with a two-element non-ideal half-wave dipole array with a transmission frequency of 28 GHz and a transmit power of 10 mW, and.

In Fig. 8, we perform a beam sweep as in Section IV and compare the simulated average PD from HFSS with the average PD predicted by the model in (55). The regions were uniformly sampled with $\epsilon = 10$ mW/cm^2, resulting in 45 and 29 sample points for $\mathcal{P}_1$ and $\mathcal{P}_2$, respectively. The proposed model approximates the simulated values well even though the value of ϵ is relatively large.

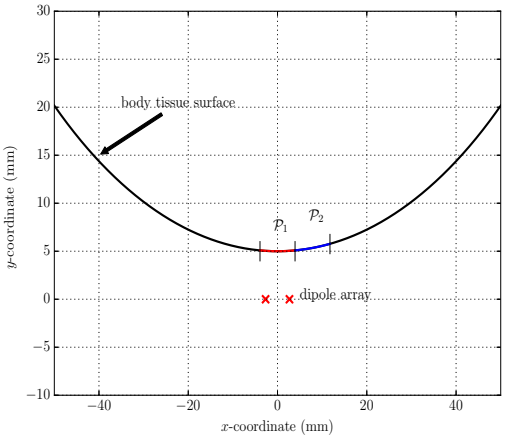

Fig. 7. Two regions considered in the validation of the average exposure model. Each region is an arc of measure 5° on the surface of a spherical head model with radius 90 mm at a distance of 5 mm from the center of the array.

We also studied the convergence of the average exposure matrix in (60) as M increases for both uniform and non-uniform samplings of the regions $\mathcal{P}_1$ and $\mathcal{P}_2$. In this case, we consider an ideal two-element half-wave dipole array and compute average PD matrices. For each region $\mathcal{P}$, the limit as $M \to \infty$ of the average PD matrices, denoted as $\mathbf{R}(\mathcal{P})$, is taken to be $\mathbf{R}_{\mathsf{EXP},\,\mathsf{avg}}(\mathcal{P})$ from (60) with $\epsilon = 0.1$ mW/cm^2. In Fig. 9, we compare the mean-square-error (MSE) between the average PD matrix $\mathbf{R}_{\mathsf{PD},\,\mathsf{avg}}(\mathcal{P})$ from (60) and $\mathbf{R}(\mathcal{P})$ versus the number of samples used to compute $\mathbf{R}_{\mathsf{PD},\,\mathsf{avg}}(\mathcal{P})$. Since the sampling procedures are defined in terms of ϵ rather than the number of samples, there is a range of values of ϵ for which a sampling of $\mathcal{P}$ will result in a fixed M. Therefore, for any given M we take the MSE above to be the average MSE among all ϵ which result in M samples. The plot shows that non-uniform sampling leads to a lower MSE than uniform-sampling in both regions. This is because the non-uniform sampling procedure allocates more samples to the portions of a region which have a larger effect on the average PD matrix than to the portions which are less impactful.

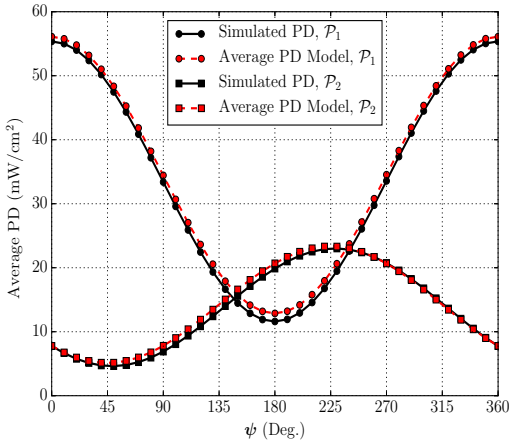

Fig. 8. Average PD values obtained from HFSS simulations using (48), and the proposed average exposure model in (55), vs. the beam sweep angle ψ of the transmit signal $\mathbf{x}$ in (29) on the regions $\mathcal{P}_1$ and $\mathcal{P}_2$. Values were obtained for a non-ideal two-element dipole array. For both regions, the proposed model was calculated using a uniform sampling with $\epsilon = 10$ mW/cm^2.

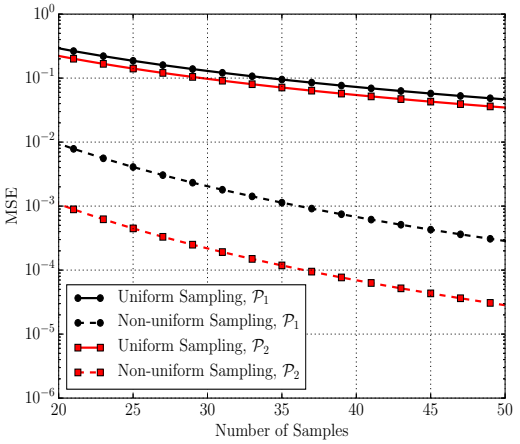

Fig. 9. Mean-square-error (MSE) between the average PD matrices $\mathbf{R}_{\mathsf{PD},\,\mathsf{avg}}(\mathcal{P})$ from (60) and $\mathbf{R}(\mathcal{P})$ vs. the number of samples M. Computations were performed for an ideal two-element dipole array.

VI. Conclusion

In this study, we examined exposure models for two major measures of electromagnetic absorption at millimeter wave frequencies. We developed expressions to approximate the pointwise exposure matrices for both incident PD and surface SAR and showed that both exposure measures are characterized by an effective steering vector. The proposed models only require a relatively small number of parameters to be computed and can predict exposure over contiguous regions without additional measurements. Software simulations demonstrate that the exposure models can estimate pointwise exposure with high accuracy.

The models were then analyzed in order to provide insights into how to sample them to obtain an accurate representation of exposure over a spatial region. The proposed uniform and non-uniform sampling guidelines indicate what inter-point

sampling distance is required to ensure that spatial exposure variations lie beneath a chosen threshold. A numerical example showing the application of the sampling algorithms demonstrates that non-uniform spatial sampling results in significantly fewer sample points. The sampling methods can further be applied to the problem of calculating quadratic models for spatially average exposure. Simulation results demonstrate that these models can effectively approximate average exposure. can be directly incorporated into exposure-aware signal design algorithms in the literature to achieve high data rates while remaining compliant with regulatory exposure standards.

VII. Appendix

A. Proof for Lemma 1

Let $r = \|\mathbf{p}\|$ and $\tilde{r} = \|\tilde{\mathbf{p}}\|$, and denote $\mathbf{a}(\mathbf{p})$ and $\mathbf{a}(\tilde{\mathbf{p}})$ as $\mathbf{a}$ and $\tilde{\mathbf{a}}$, respectively. The n-th element of $\mathbf{a}$ is expressed as

$$\mathbf{a}_n = g_n^{1/2}(\mathbf{p}_n)\frac{r}{r_n}\exp\left(-j\varphi_n\right), \tag{62}$$

where φ_n is given as in (5), and similarly for $\tilde{\mathbf{a}}_n$. Since the points $\mathbf{p}$ and $\tilde{\mathbf{p}}$ are nonzero, the desired bound can be expressed as

$$A = \frac{\left|\left|\tilde{r}\mathbf{a}^H\mathbf{x}\right| - \left|r\tilde{\mathbf{a}}^H\mathbf{x}\right|\right|}{r\tilde{r}}\frac{\left|\tilde{r}\mathbf{a}^H\mathbf{x}\right| + \left|r\tilde{\mathbf{a}}^H\mathbf{x}\right|}{r\tilde{r}} < \varepsilon. \tag{63}$$

We first derive an upper bound on A in terms of the inter-point distance $\|\mathbf{p}-\tilde{\mathbf{p}}\|$. An application of the reverse triangle inequality and the Cauchy-Schwarz inequality gives an upper bound on A as

$$A \le BC\|\mathbf{x}\|^2 \triangleq \left[\frac{\|\tilde{r}\mathbf{a} - r\tilde{\mathbf{a}}\|}{r\tilde{r}}\right]\left[\frac{\|\tilde{r}\mathbf{a}\| + \|r\tilde{\mathbf{a}}\|}{r\tilde{r}}\right]\|\mathbf{x}\|^2. \tag{64}$$

For clarity, we bound B and C separately.

Through repeated applications of the triangle inequality and the Cauchy-Schwarz inequality, it can be shown that the term B can be bounded as

$$\begin{aligned}
B &\le G_{\mathsf{max}}^{1/2}\sum_{n=0}^{N-1}\left|\frac{\exp(j\varphi_n)}{r_n} - \frac{\exp(j\tilde{\varphi}_n)}{\tilde{r}_n}\right| \\
&\le G_{\mathsf{max}}^{1/2}\sum_{n=0}^{N-1}\left(\frac{1}{r_n}\left|\exp(j\varphi_n) - \exp(j\tilde{\varphi}_n)\right| + \left|\frac{1}{r_n} - \frac{1}{\tilde{r}_n}\right|\right) \\
&= G_{\mathsf{max}}^{1/2}\sum_{n=0}^{N-1}\left(\frac{2}{r_n}\left|\sin\left(\frac{\varphi_n - \tilde{\varphi}_n}{2}\right)\right| + \left|\frac{\tilde{r}_n - r_n}{r_n\tilde{r}_n}\right|\right) \\
&\overset{(a)}{<} G_{\mathsf{max}}^{1/2}\sum_{n=0}^{N-1}\left(\frac{2\pi}{\lambda r_n}|r_n - r + \tilde{r} - \tilde{r}_n| + \left|\frac{\tilde{r}_n - r_n}{r_n\tilde{r}_n}\right|\right) \\
&\le G_{\mathsf{max}}^{1/2}\sum_{n=0}^{N-1}\left(\frac{2\pi}{\lambda r_n}\left(|r_n - \tilde{r}_n| + |r - \tilde{r}|\right) + \left|\frac{\tilde{r}_n - r_n}{r_n\tilde{r}_n}\right|\right) \\
&\overset{(b)}{\le} G_{\mathsf{max}}^{1/2}\left(\frac{4\pi N}{r_{\mathsf{min}}\lambda}\|\mathbf{p}-\tilde{\mathbf{p}}\| + \frac{N}{r_{\mathsf{min}}^2}\|\mathbf{p}-\tilde{\mathbf{p}}\|\right),
\end{aligned} \tag{65}$$

The bound $\sin(y) < y$ for $y > 0$ is used in (a), and (b) results from the definition of r_{min}. Similarly, the term C can be bounded as

$$\begin{aligned}
C &\le G_{\mathsf{max}}^{1/2}\sum_{n=0}^{N-1}\left(\left|\frac{\exp(j\varphi_n)}{r_n}\right| + \left|\frac{\exp(j\tilde{\varphi}_n)}{\tilde{r}_n}\right|\right) \\
&\le \frac{2NG_{\mathsf{max}}^{1/2}}{r_{\mathsf{min}}}.
\end{aligned} \tag{66}$$

Combining the bounds for B and C, we have that

$$A < \frac{2N^2G_{\mathsf{max}}\|\mathbf{x}\|^2}{r_{\mathsf{min}}^2}\left(\frac{4\pi}{\lambda} + \frac{1}{r_{\mathsf{min}}}\right)\|\mathbf{p}-\tilde{\mathbf{p}}\|. \tag{67}$$

Therefore, $A < \varepsilon$ if

$$\|\mathbf{p}-\tilde{\mathbf{p}}\| < \frac{\varepsilon r_{\mathsf{min}}^2}{2N^2G_{\mathsf{max}}\|\mathbf{x}\|^2}\left(\frac{4\pi}{\lambda} + \frac{1}{r_{\mathsf{min}}}\right)^{-1}. \tag{68}$$

References

[1] M. R. Castellanos, D. J. Love, and B. M. Hochwald, "Hybrid precoding for millimeter wave systems with a constraint on user electromagnetic radiation exposure," in *Proc. IEEE Asilomar Conf. Signals, Systems, and Computers*, Pacific Grove, CA, Nov. 2016, pp. 296–300.

[2] W. Roh, J.-Y. Seol, J. Park, B. Lee, J. Lee, Y. Kim, J. Cho, K. Cheun, and F. Aryanfar, "Millimeter-wave beamforming as an enabling technology for 5g cellular communications: Theoretical feasibility and prototype results," *IEEE Commun. Mag.*, vol. 52, no. 2, pp. 106–113, Feb. 2014.

[3] A. Ghosh, T. A. Thomas, M. C. Cudak, R. Ratasuk, P. Moorut, F. W. Vook, T. S. Rappaport, G. R. MacCartney, S. Sun, and S. Nie, "Millimeter-wave enhanced local area systems: A high-data-rate approach for future wireless networks," *IEEE Journ. Sel. Areas in Commun.*, vol. 32, no. 6, pp. 1152–1163, June 2014.

[4] T. S. Rappaport, S. Sun, R. Mayzus, H. Zhao, Y. Azar, K. Wang, G. N. Wong, J. K. Schulz, M. Samimi, and F. Gutierrez Jr, "Millimeter wave mobile communications for 5g cellular: It will work!" *IEEE Access*, vol. 1, no. 1, pp. 335–349, May 2013.

[5] S. Hur, T. Kim, D. J. Love, J. V. Krogmeier, T. A. Thomas, and A. Ghosh, "Millimeter wave beamforming for wireless backhaul and access in small cell networks," *IEEE Trans. Commun.*, vol. 61, no. 10, pp. 4391–4403, Oct. 2013.

[6] C. Dehos, J. L. González, A. De Domenico, D. Ktenas, and L. Dussopt, "Millimeter-wave access and backhauling: the solution to the exponential data traffic increase in 5g mobile communications systems?" *IEEE Commun. Mag.*, vol. 52, no. 9, pp. 88–95, Sept. 2014.

[7] J. Choi, V. Va, N. Gonzalez-Prelcic, R. Daniels, C. R. Bhat, and R. W. Heath, "Millimeter-wave vehicular communication to support massive automotive sensing," *IEEE Commun. Mag.*, vol. 54, no. 12, pp. 160–167, Dec. 2016.

[8] J. Hasch, E. Topak, R. Schnabel, T. Zwick, R. Weigel, and C. Waldschmidt, "Millimeter-wave technology for automotive radar sensors in the 77 ghz frequency band," *IEEE Trans. Microw. Theory Tech.*, vol. 60, no. 3, pp. 845–860, Mar. 2012.

[9] O. El Ayach, S. Rajagopal, S. Abu-Surra, Z. Pi, and R. W. Heath, "Spatially sparse precoding in millimeter wave mimo systems," *IEEE Trans. Wireless Commun.*, vol. 13, no. 3, pp. 1499–1513, Mar. 2014.

[10] J. Brady, N. Behdad, and A. M. Sayeed, "Beamspace mimo for millimeter-wave communications: System architecture, modeling, analysis, and measurements," *IEEE Trans. Antennas Propag.*, vol. 61, no. 7, pp. 3814–3827, July 2013.

[11] A. Alkhateeb, O. El Ayach, G. Leus, and R. W. Heath, "Channel estimation and hybrid precoding for millimeter wave cellular systems," *IEEE Journ. Sel. Topics in Sig. Proc.*, vol. 8, no. 5, pp. 831–846, Oct. 2014.

[12] V. Raghavan, J. Cezanne, S. Subramanian, A. Sampath, and O. Koymen, "Beamforming tradeoffs for initial ue discovery in millimeter-wave mimo systems," *IEEE Journ. Sel. Topics in Sig. Proc.*, vol. 10, no. 3, pp. 543–559, Apr. 2016.

[13] J. Song, J. Choi, S. G. Larew, D. J. Love, T. A. Thomas, and A. A. Ghosh, "Adaptive millimeter wave beam alignment for dual-polarized mimo systems," *IEEE Trans. Wireless Commun.*, vol. 14, no. 11, pp. 6283–6296, Nov. 2015.

[14] S. Noh, M. D. Zoltowski, and D. J. Love, "Multi-resolution codebook and adaptive beamforming sequence design for millimeter wave beam alignment," *IEEE Trans. Wireless Commun.*, vol. 16, no. 9, pp. 5689–5701, June 2017.

[15] J. Song, J. Choi, and D. J. Love, "Common codebook millimeter wave beam design: Designing beams for both sounding and communication with uniform planar arrays," *IEEE Trans. Commun.*, vol. 65, no. 4, pp. 1859–1872, Apr. 2017.

[16] M. R. Castellanos, V. Raghavan, J. H. Ryu, O. H. Koymen, J. Li, D. J. Love, and B. Peleato, "Channel-reconstruction-based hybrid precoding for millimeter-wave multi-user MIMO systems," *IEEE Journ. Sel. Topics in Sig. Proc.*, vol. 12, no. 2, pp. 383–398, May 2018.

[17] World Health Organization, International Agency for Research on Cancer, "IARC classifies radiofrequency electromagnetic fields as possibly carcinogenic to humans," http://www.iarc.fr/en/media centre/pr/2011/pdfs/pr208_E.pdf, May 2011.

[18] "Evaluating compliance with FCC guidelines for human exposure to radiofrequency electromagnetic fields," Federal Communications Commission, Tech. Rep. OET Bull. 65, Suppl. C, ed. 01-01, June 2001.

[19] ICNIRP, "Guidelines for limiting exposure to time-varying electric, magnetic, and electromagnetic fields (up to 300 ghz)," *Health Phys.*, vol. 74, no. 4, pp. 494–521, Apr. 1998.

[20] *IEEE Standard for Safety Levels with Respect to Human Exposure to Radio Frequency Electromagnetic Fields, 3 kHz to 300 GHz*. IEEE Standard C95.1-2005, 2005.

[21] M. Zhadobov, N. Chahat, R. Sauleau, C. Le Quement, and Y. Le Drean, "Millimeter-wave interactions with the human body: state of knowledge and recent advances," *Int. J. Microw. Wirel. Technol.*, vol. 3, no. 02, pp. 237–247, Apr. 2011.

[22] T. Wu, T. S. Rappaport, and C. M. Collins, "Safe for generations to come: Considerations of safety for millimeter waves in wireless communications," *IEEE Microw. Mag.*, vol. 16, no. 2, pp. 65–84, Mar. 2015.

[23] D. Colombi, B. Thors, and C. Törnevik, "Implications of EMF exposure limits on output power levels for 5G devices above 6 ghz," *IEEE Antennas Wireless Propag. Lett.*, vol. 14, pp. 1247–1249, 2015.

[24] K. Zhao, Z. Ying, and S. He, "EMF exposure study concerning mmwave phased array in mobile devices for 5G communication," *IEEE Antennas Wireless Propag. Lett.*, vol. 15, pp. 1132–1135, 2016.

[25] B. Thors, D. Colombi, Z. Ying, T. Bolin, and C. Törnevik, "Exposure to RF EMF from array antennas in 5g mobile communication equipment," *IEEE Access*, vol. 4, pp. 7469–7478, Aug. 2016.

[26] I. Nasim and S. Kim, "Mitigation of human RF exposure in 5G downlink," *arXiv preprint arXiv:1807.09094*, Jan. 2018.

[27] M. Mangoud, R. Abd-Alhameed, N. McEwan, P. Excell, and E. Abdulmula, "SAR reduction for handset with two-element phased array antenna computed using hybrid MoM/FDTD technique," *Electron. Lett.*, vol. 35, no. 20, pp. 1693–1694, Sept. 1999.

[28] K.-C. Chim, K. C. Chan, and R. D. Murch, "Investigating the impact of smart antennas on SAR," *IEEE Trans. Antennas Propag.*, vol. 52, no. 5, pp. 1370–1374, May 2004.

[29] B. M. Hochwald and D. J. Love, "Minimizing exposure to electromagnetic radiation in portable devices," in *UCSD Information Theory Appl. Workshop (ITA)*, San Diego, CA, Feb. 2012, pp. 255–261.

[30] B. M. Hochwald, D. J. Love, S. Yan, and J. Jin, "SAR codes," in *UCSD Information Theory Appl. Workshop (ITA)*, San Diego, CA, Feb. 2013, pp. 1–9.

[31] B. M. Hochwald, D. J. Love, S. Yan, P. Fay, and J. M. Jin, "Incorporating specific absorption rate constraints into wireless signal design," *IEEE Commun. Mag.*, vol. 52, no. 9, pp. 126–133, Sept. 2014.

[32] A. Ebadi-Shahrivar, J. Ren, B. M. Hochwald, P. Fay, J.-M. Jin, and D. J. Love, "Mixed quadratic model for peak spatial-average sar of coherent multiple antenna devices," in *Proc. IEEE Int. Symp. Antennas and Propagation USNC/URSI Nat. Radio Science Meeting*, San Diego, CA, July 2017, pp. 1419–1420.

[33] J. Li, S. Yan, Y. Liu, B. M. Hochwald, and J. M. Jin, "A high-order model for fast estimation of electromagnetic absorption induced by multiple transmitters in portable devices," *IEEE Trans. Antennas Propag.*, vol. 65, no. 12, pp. 6768–6778, Dec. 2017.

[34] A. Ebadi-Shahrivar, P. Fay, B. M. Hochwald, and D. J. Love, "Multi-antenna SAR estimation in linear time," presented at the IEEE Int. Symp. Antennas and Propagation USNC/URSI Nat. Radio Science Meeting, Boston MA, July, 2018.

[35] A. Ebadi-Shahrivar, P. Fay, D. J. Love, and B. M. Hochwald, "Determining electromagnetic exposure compliance of multi-antenna devices in linear time," *Submitted to IEEE Trans. Antennas Propag.*, Feb. 2018.

[36] D. Ying, D. J. Love, and B. M. Hochwald, "Closed-loop precoding and capacity analysis for multiple antenna wireless systems with user radiation exposure constraints," *IEEE Trans. Wireless Commun.*, vol. 14, no. 10, pp. 5859–5870, Oct. 2015.

[37] D. Ying, D. J. Love, and B. M. Hochwald, "Sum-rate analysis for multi-user mimo systems with user exposure constraints," *IEEE Trans. Wireless Commun.*, vol. 16, no. 11, pp. 7376–7388, Sept. 2017.

[38] D. Ying, D. J. Love, and B. M. Hochwald, "Beamforming optimization with a constraint on user electromagnetic radiation exposure," in *Proc. Conf. Information Sciences and Systems (CISS)*, Baltimore, MD, Mar. 2013.

[39] D. Ying, D. J. Love, and B. M. Hochwald, "Transmit covariance optimization with a constraint on user electromagnetic radiation exposure," in *Proc. IEEE Global Communications Conf. (GLOBECOM)*, Atlanta, GA, Dec. 2013, pp. 4104–4109.

[40] J. C. Lin, "Specific absorption rates induced in head tissues by microwave radiation from cell phones," *IEEE Microw. Mag.*, vol. 2, no. 1, pp. 22–25, Oct. 2001.

[41] D. H. Johnson and D. E. Dudgeon, *Array Signal Processing: Concepts and Techniques*. Eaglewood Cliffs, NJ, USA: PTR Prentice Hall, 1993.

[42] O. P. Gandhi and A. Riazi, "Absorption of millimeter waves by human beings and its biological implications," *IEEE Trans. Microw. Theory Tech.*, vol. 34, no. 2, pp. 228–235, Feb. 1986.

[43] S. Gabriel, R. Lau, and C. Gabriel, "The dielectric properties of biological tissues: Ii. measurements in the frequency range 10 hz to 20 ghz," *Phys. Med. Biol.*, vol. 41, no. 11, p. 2251, Nov. 1996.

[44] S. Alekseev and M. Ziskin, "Human skin permittivity determined by millimeter wave reflection measurements," *Bioelectromagnetics*, vol. 28, no. 5, pp. 331–339, July 2007.

[45] N. Chahat, M. Zhadobov, L. Le Coq, S. I. Alekseev, and R. Sauleau, "Characterization of the interactions between a 60-ghz antenna and the human body in an off-body scenario," *IEEE Trans. Antennas Propag.*, vol. 60, no. 12, pp. 5958–5965, Dec. 2012.

[46] C. A. Balanis, *Antenna Theory: Analysis and Design*, 4th ed. Hoboken, NJ: John Wiley & Sons, Inc., 2016.

[47] *IEEE Recommended Practice for Measurements and Computations of Radio Frequency Electromagnetic Fields With Respect to Human Exposure to Such Fields, 100 kHz-300 GHz*. IEEE Standard C95.3-2002, 2002.

[48] I. Gupta and A. Ksienski, "Effect of mutual coupling on the performance of adaptive arrays," *IEEE Trans. Antennas Propag.*, vol. 31, no. 5, pp. 785–791, Sept. 1983.

[49] B. Friedlander and A. J. Weiss, "Direction finding in the presence of mutual coupling," *IEEE Trans. Antennas Propag.*, vol. 39, no. 3, pp. 273–284, Mar. 1991.

[50] T. Su and H. Ling, "On modeling mutual coupling in antenna arrays using the coupling matrix," *Microw. Opt. Tech. Lett.*, vol. 28, no. 4, pp. 231–237, Feb. 2001.

[51] M. Born and E. Wolf, *Principles of optics*, 7th ed. Cambridge, UK: Cambridge Univ. Press, 1999.